nature communications

Article

https://doi.org/10.1038/s41467-026-73143-8

Interpretable deep learning framework for mapping E3–substrate binding interfaces

Received: 16 October 2025

Accepted: 5 May 2026

Published online: 20 May 2026

Check for updates

Dianke Li (李点可)[1,2,3,4], Yuting Zhang (张雨婷)[2,4], Yuan Liu (刘源)[2,4], Zihao Zhang (张梓昊)[1], Yingjie Qu (瞿英杰)[2,3], Jiajun Li (李佳俊)[1], Linyang Jiang (江临洋)[1], Lihong Diao (刁丽红)[2,3], Ziding Zhang (张子丁)[1] ✉, Lingqiang Zhang (张令强)[2] ✉, Chun-Ping Cui (崔春萍)[2] ✉ & Dong Li (李栋)[2] ✉

E3 ubiquitin ligases recognize substrates through specific interfaces. Accurate delineation of these interfaces is essential, as mutations disrupting them impair protein ubiquitination and drive cancer progression. However, available E3–substrate interface data are sparse and systematic prediction methods remain lacking. Here, we propose MetaESI, a deep learning framework that simultaneously predicts E3–substrate interactions and leverages its interpretable architecture to infer binding interfaces de novo. With a two-stage meta-learning strategy, MetaESI generalizes across diverse E3s and achieves state-of-the-art performance in both interaction and interface prediction. We applied MetaESI at the proteome scale to generate MetaESI-Atlas, which comprises 68,056 annotated interactions across eight species. Integrating multi-omics data, we identified mutations at MetaESI-predicted interfaces that disrupt E3–substrate binding, and experimentally validated representative examples including JunB Q244E and SPOP F102C as oncogenic drivers. By combining interpretable AI with mechanistic insight, MetaESI establishes a methodological paradigm for interpretable model design and a foundational resource for precision oncology and targeted protein degradation.

E3 ubiquitin ligases (E3s) mediate selective protein degradation by recognizing target substrates and catalyzing their ubiquitination[1]. This recognition relies on precise, structurally complementary interfaces between E3s and their substrates[2]. Oncogenic mutations disrupting these interfaces (either in substrates or E3s) impair protein degradation, contributing to cancer progression. Substrate-interface mutations typically evade degradation, elevating oncoprotein abundance[3,4], while E3-interface mutations impair substrate targeting, leading to pathological stabilization of multiple cancer drivers[5]. These mechanisms highlight the urgent need to systematically map E3–substrate interfaces. Elucidating these interfaces serves two pivotal purposes: (1) enabling comprehensive dissection of oncogenic mutations that disrupt these interfaces, thereby clarifying tumorigenic mechanisms and revealing actionable therapeutic targets for precision oncology[6–8]; (2) providing the structural foundation for rational drug design, particularly by advancing targeted protein degradation technologies (e.g., PROTACs, molecular glues)[9–11].

Despite their established significance, proteome-wide mapping of E3–substrate interfaces remains a major challenge. Experimental approaches (e.g., structural biology[12], alanine scanning[13]) suffer from inherently low throughput, resulting in severe scarcity of E3–substrate interface data for computational model training. Consequently, existing computational tools (e.g., our prior UbiBrowser[14], TransESI[15]) primarily

[1]State Key Laboratory of Animal Biotech Breeding, College of Biological Sciences, China Agricultural University, Beijing, China. [2]State Key Laboratory of Medical Proteomics, National Center for Protein Sciences (Beijing), Academy of Military Medical Sciences, Beijing, China. [3]Laboratory of Biological Networks, Beijing Proteome Research Center, Beijing, China. [4]These authors contributed equally: Dianke Li, Yuting Zhang, Yuan Liu. ✉e-mail: zidingzhang@cau.edu.cn; zhanglq@nic.bmi.ac.cn; cui_chunping2000@aliyun.com; lidong.bprc@foxmail.com

predict interacting pairs but fail to provide residue-level interface details essential for mechanistic insight and mutation interpretation. This fundamental limitation is reflected in the stark contrast between database coverages. While repositories cataloging E3–substrate pairs are extensive (e.g., UbiBrowser 2.0[16] contains >4000 entries), those documenting interfaces are remarkably scarce (e.g., ELM[17] curates only ~23 motifs relevant to E3-mediated degradation). Therefore, given this paucity of experimental data for training, developing novel methodologies capable of systematically identifying specific binding interfaces de novo is imperative. In this context, interpretable deep learning models offer a promising solution[18–22]. While prior work used interpretability to uncover diverse biological mechanisms, we uniquely harness it for de novo inference of E3–substrate binding interfaces.

Here, we present MetaESI, an interpretable deep learning framework that, by design, simultaneously predicts E3–substrate interactions (ESIs) and infers their binding interfaces de novo. MetaESI embeds biophysical principles into its architecture to generate residue-level interface maps, enabling each prediction to be traced to biologically meaningful hotspots. MetaESI employs a two-stage adaptive learning strategy: a meta-learning phase extracts transferable knowledge across diverse E3s, followed by an E3-specific transfer phase that adapts this knowledge to predict interactions for individual E3s. Through rigorous benchmarking, MetaESI achieved state-of-the-art ESI prediction and even outperformed complex structure prediction methods such as AlphaFold3[23] and ESMFold[24] in residue-level interface prediction. Leveraging this capability, we constructed the MetaESI-Atlas (68,056 interactions; Supplementary Data 1) with residue-level interface annotations.

Through multi-omics interrogation of this atlas, MetaESI systematically identified oncogenic E3–substrate interface mutations, several of which we experimentally validated. Together, these findings establish MetaESI as a proteome-wide framework systematically linking mutation hotspots, substrate dysregulation, and oncogenic phenotypes, thereby providing a valuable resource for subtype-specific target discovery in precision oncology. The open-source code for MetaESI is available at https://github.com/LiDlab/MetaESI.

Results

Interpretable architecture of MetaESI

To design an interpretable architecture, we first considered domain priors available to the model. We analyzed E3–substrate binding interfaces and observed a consistent principle, structured E3 regions engage disordered substrate regions (see Supplementary Notes). This order-disorder complementarity motivated the development of MetaESI, an interpretable deep learning framework that predicts E3–substrate interactions and infers their binding interfaces de novo.

MetaESI consists of two synergistic modules. The preprocessing module identifies candidate interface regions by integrating AlphaFold-predicted structures with our Graph-Aware Residue Depth (GARD) metric (Fig. 1a and "Methods"). Structured E3 domains (GARD > 1.5) are treated as potential "keyholes", while disordered substrate motifs (GARD ≤ 1.5) are considered potential "key teeth". This biologically informed preprocessing constrains subsequent operations to regions with the highest interaction potential, eliminating noise from non-functional areas.

The interpretable architecture module then simulates the spatially localized nature of lock-key recognition through locality-constrained feature aggregation (Fig. 1b). MetaESI first encodes the primary sequences of both E3 and substrate into residue-level embeddings using the protein language model ESM2[24]. Subsequently, feature extraction and aggregation are performed precisely over these constrained regions defined by preprocessing. For substrate disordered regions, a truncated transformer[25] aggregates features solely based on short-range dependencies (e.g., local sequence patterns within motifs) to generate a substrate "key representation" (see "Methods"). Concurrently, for E3 structured regions, a multi-layer graph attention network (GAT)[26] performs domain-aware feature aggregation guided by the E3 residue contact map[27]. Each residue integrates information only from neighboring residues defined by the contact map, yielding an E3 "lock representation".

To capture biophysical complementarity, a dot-product decoder computes compatibility scores between the substrate key and E3 lock representations, quantifying their potential chemical and geometric match. The resulting scores form an interpretable interface map of predicted residue–residue interaction probabilities. Within this map, high-probability hotspots pinpoint residues likely forming the binding interface (Fig. 1b). Finally, a pooling operation on this interface map yields a holistic interaction prediction score. MetaESI provides inherent interpretability, as each prediction can be directly traced to localized interaction scores in the interface map, allowing clear identification of structural features that drive binding.

Adaptive learning strategy of MetaESI

To ensure MetaESI performs reliably across diverse E3s, we curated a comprehensive ESI dataset for model training (see "Methods"). This dataset exhibits a pronounced long-tailed distribution of substrate counts per E3 (Fig. 1c), where data imbalance hinders accurate prediction of binding specificity for E3s with scarce known substrates. To address this challenge, we developed a two-stage adaptive learning strategy that dynamically adjusts the training paradigm according to substrate data availability[28,29]. E3s were categorized into three classes based on substrate counts: Common (>4 substrates), Few (2–4 substrates), and Rare (single substrate), each corresponding to a customized adaptation strategy. This two-stage strategy operates hierarchically: meta-learning first captures universal interaction patterns, while E3-specific transfer learning fine-tunes them to individual E3s, balancing generalization with specificity.

During the meta-learning phase, we implemented a modified Model-Agnostic Meta-Learning (MAML[30]) framework (Fig. 1d). In each training episode, E3-specific tasks are generated through random sampling, and each task is individually divided into a support set and a query set. The support set is used to adapt the meta-learner parameters, thereby generating a task-specific model. The query set is used to evaluate predictive performance and compute the corresponding task-specific loss. Losses across all tasks are then aggregated to update the meta-learner parameters. This episodic training scheme, simulating multiple adaptation scenarios, is designed to endow the meta-learner with strong generalization capability, enabling rapid adaptation to new E3-specific prediction tasks with minimal samples. In the subsequent E3-specific transfer phase, distinct optimization strategies are applied based on E3 category (Fig. 1e). For Common E3s, the meta-learner is further trained using abundant substrate data. For few E3s, the meta-learner is fine-tuned with limited samples. For Rare E3s, the meta-learner is adapted using data from highly similar E3s identified by cosine similarity of their representations.

This hierarchical learning strategy ensures comprehensive ESI prediction across all E3s, regardless of limited substrate data availability. Remarkably, it mirrors human learning mechanisms. The meta-learning stage accumulates transferable knowledge, much like how humans acquire diverse experiences. In turn, the transfer learning stage enables rapid adaptation to new tasks by leveraging analogical reasoning, similar to how humans apply prior knowledge in unfamiliar scenarios.

MetaESI accurately predicts E3–substrate interactions

To rigorously evaluate MetaESI's ESI prediction capability, we constructed gold-standard datasets for Common, Few, and Rare E3 categories (Supplementary Data 2). These datasets model three key scenarios: discovery of novel substrates for well-studied E3s (Common), guidance for wet-lab research on defined E3s (Few), and deorphanization of orphan E3s (Rare). MetaESI was benchmarked against:

https://doi.org/10.1038/s41467-026-73143-8

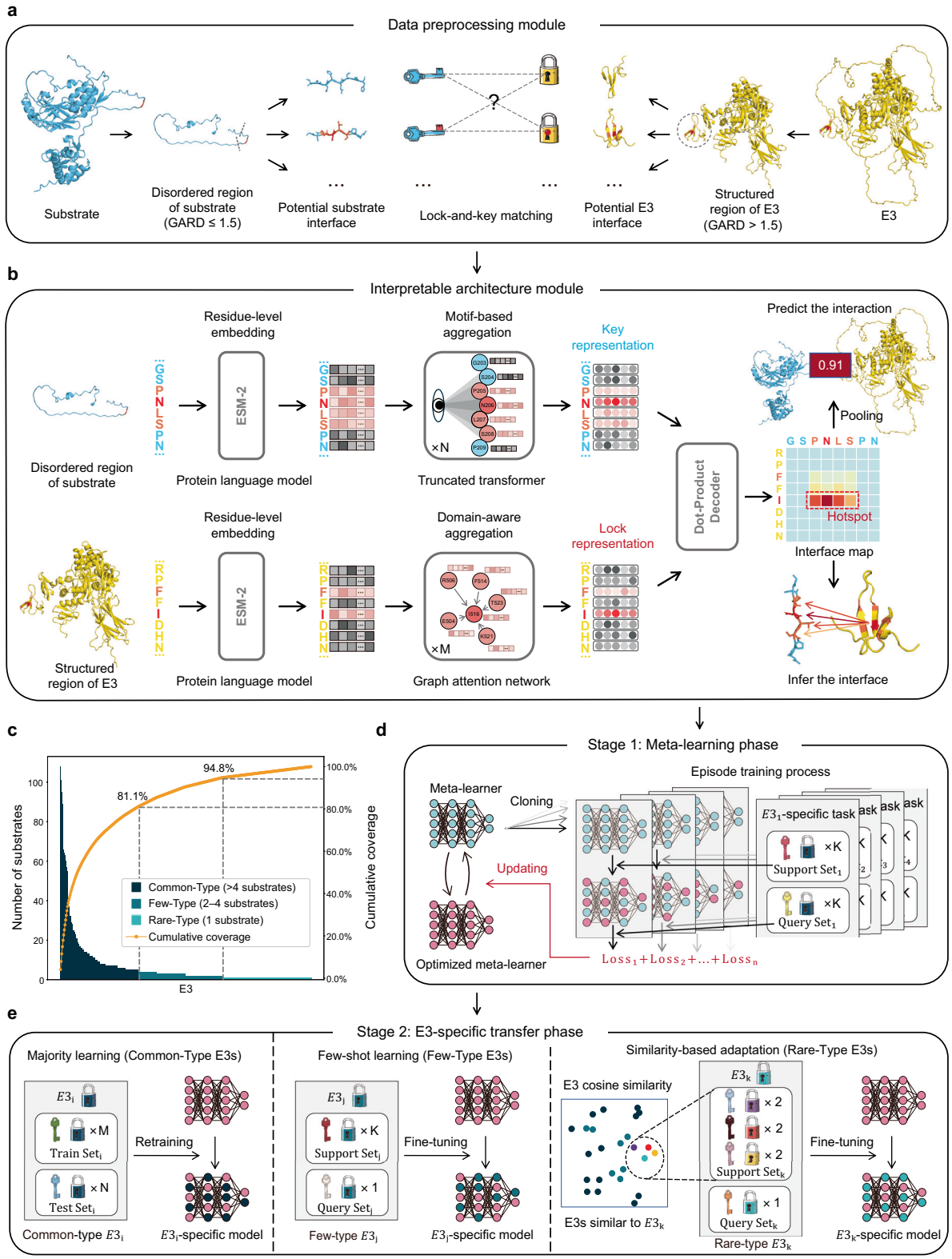

(1) specialized ESI prediction tools (UbiBrowser 2.0/UB2[16], TransESI[15]), (2) general protein–protein interaction (PPI) prediction tools (HIGH-PPI[31], SGPPI[32], PIPR[33]), (3) classical machine learning algorithms (SVM, RF, KNN, LR, XGBoost), and (4) structural docking methods (ZDOCK[34], Rosetta[35]). MetaESI robustly outperformed all baselines across all four categories (Fig. 2a, b and Supplementary Figs. 1 and 2), achieving AUROC/AUPRC scores of 0.85/0.71 (Common), 0.82/0.65 (Few), and 0.73/0.59 (Rare), with strong performance even in the most challenging data-sparse Rare category.

Benchmark experiment further highlights MetaESI's unique strengths. It significantly outperformed TransESI (which uses transfer learning) in data-scarce Few/Rare tasks, demonstrating the superiority of its meta-learning strategy for few-shot tasks. Conversely, HIGH-PPI (reliant on PPI network topology) performed acceptably only for Common

Fig. 1 | Architecture and learning strategy of MetaESI. a MetaESI utilizes GARD metrics to screen potential binding-mediating regions within E3 and substrate structures. This process identifies complementary features that enable precise lock-and-key matching through MetaESI's interpretable architecture. **b** Interpretable architecture of MetaESI. Substrate sequences are encoded by ESM2 and processed through a truncated transformer to generate "key" representations. E3 sequences (ESM2 encoded) with tertiary structures are processed through a graph attention network to generate "lock" representations. The lock-and-key matching is performed via a dot-product decoder, producing an "interface map" that jointly predicts interaction probabilities and infers binding interface residues. **c** Substrate distribution of E3s. E3s are classified into three types: Common (> 4 substrates, $n = 122$ E3s), Few (2–4 substrates, $n = 130$ E3s), and Rare (single substrate, $n = 138$ E3s). Bars represent substrate counts (left axis), while the orange curve illustrates cumulative substrate coverage (right axis). **d** During the meta-learning phase, the meta-learner clones multiple model instances, each of which is independently trained and evaluated on distinct E3-specific tasks. The aggregated losses from these tasks are then used to update the meta-learner. **e** During the E3-specific transfer phase, the optimized meta-learner adapts based on E3 type: Common-Type $E3_i$ employs many-shot learning (re-training with abundant $E3_i$-specific samples); Few-Type $E3_j$ uses few-shot learning (fine-tuning with limited $E3_j$-specific samples); Rare-Type $E3_k$ applies similarity-based adaptation (by fine-tuning with samples from similar E3s), simulating a zero-shot setting.

E3s, showing severe performance decrease for Few/Rare categories. This highlights how topological sparsity in understudied E3 classes limits network-based methods and underscores MetaESI's robustness.

Ablation experiments elucidated the key factors driving model performance (Supplementary Fig. 3). Sequence context, structural features, and GARD metrics all contribute substantially to predictions in the Common category. Meanwhile, the meta-learning stage is critical for Few/Rare performance. Comparing MetaESI to an ablated variant lacking meta-learning (MetaESI w/o Meta) revealed substantial performance gains across diverse few-shot scenarios, including ESIs mediated by different E3 families, distinct ubiquitin chain modifications, and cross-species predictions (Fig. 2c). Further analysis revealed synergistic complementarity between meta-learning task volume (M) and fine-tuning sample size (K). Increases in M enhanced cross-task generalization, while additional K samples improved adaptation to specific E3s (Supplementary Fig. 4). These findings suggest that the meta-learning and few-shot learning stages work synergistically, with the former establishing generalized knowledge and the latter enabling E3-specific adaptations, together driving MetaESI's superior performance in data-scarce scenarios.

Leveraging MetaESI's robust performance, we performed a proteome-wide scan to construct the MetaESI-Atlas. This resource comprises 46,579 predicted interactions between 371 human E3s and 9421 human substrates. Extending to seven additional model organisms, the atlas encompasses a total of 68,056 interactions across 675 E3s and 18,752 substrates (Supplementary Data 1). To assess the biological plausibility of MetaESI-Atlas, we evaluated Gene Ontology (GO) term similarity between E3s and their predicted substrates in terms of both biological process (BP) and cellular component (CC). As shown in Fig. 2d, consistent with known ESIs, human E3-predicted substrate pairs exhibited significant similarity in both BP and CC. This similarity markedly exceeded that observed for randomly sampled E3-random protein interactions (ERIs). Furthermore, in humans, E3s and their predicted substrates occupy tightly interconnected subgraphs within the PPI network (Fig. 2d). Identical patterns were observed in MetaESI-Atlas predictions for other species (Supplementary Fig. 5).

MetaESI pinpoints E3–substrate interfaces de novo

Beyond accurate ESI prediction, MetaESI's core strength lies in its ability to predict E3–substrate binding interfaces de novo, without reliance on experimental interface data for training. This capability stems from its knowledge-guided, interpretable architecture. By integrating biophysical principles (e.g., lock-and-key recognition) into the model design, MetaESI directly generates interpretable outputs. Specifically, it takes an E3–substrate pair as input and outputs a residue–residue interaction probability matrix (interface map; Fig. 3a), in which rows correspond to E3 residues and columns to substrate residues. A pooling operation then converts this map into a holistic interaction probability score, reflecting the biological principle that binding primarily depends on critical "hotspot" residues within the interface. This design drives MetaESI to learn evolutionarily conserved, biophysically critical interaction patterns, manifested as high-probability hotspots in the interface map.

To systematically evaluate MetaESI's interface prediction accuracy, we first predicted interface maps for all E3–substrate pairs in our gold-standard positive (GSP) dataset (Supplementary Data 3). We then assessed the subset with experimentally determined interfaces (Supplementary Data 4) by computing the Earth Mover's Distance (EMD[36]) between predicted and experimental interfaces. MetaESI significantly outperformed all benchmarks across three key metrics (Fig. 3b): (1) overall E3–substrate interface accuracy, (2) E3-interface accuracy, and (3) substrate interface accuracy. Benchmarks included complex structure predictors (AlphaFold3, ESMFold), protein-docking methods (ZDOCK), structure-based binding site predictors (PeSTo[37], ScanNet[38]), and a random-interface negative control. This comprehensive comparison demonstrates MetaESI's superiority in E3–substrate interface prediction. Importantly, unlike benchmark methods that rely on interface data either explicitly in training (e.g., PeSTo, ScanNet) or implicitly through complex structure databases (e.g., AlphaFold3, ESMFold), MetaESI achieves de novo interface prediction solely using ESI data.

We further analyzed representative cases to exemplify MetaESI's advantages. For the SPOP–BRD3[39] complex, MetaESI's predicted hotspots were precisely localized to the MATH domain of SPOP (Fig. 3c), which is its known substrate-binding region[40]. When these hotspots were mapped to the experimental structure, they showed near-perfect alignment with the true interface (Fig. 3d). In contrast, PeSTo produced extensive false positives, and ScanNet failed entirely (Fig. 3e). This contrast reveals a key limitation of general binding site predictors. These methods identify potential binding regions on individual proteins, but they are unable to predict specific pairwise interaction interfaces. MetaESI overcomes this limitation by directly modeling complementary E3–substrate interfaces.

For the regulated SMURF1–SMAD1[41] complex (where SMAD1 Ser214 phosphorylation alters the interface), MetaESI's hotspots localized to SMURF1's WW domain (Fig. 3f), which is a known substrate-binding region in Nedd4-family E3s[41]. These predictions closely aligned with experimental interfaces in both phosphorylated (Fig. 3g) and non-phosphorylated states (Fig. 3h). Mapping MetaESI's interface scores onto AlphaFold3-, ESMFold-, and ZDOCK-predicted complexes revealed discordance with ground truth (Fig. 3i). Complex structure prediction methods face inherent limitations in modeling interactions mediated by highly flexible regions. This is evident in their inability to accurately predict antigen–antibody interfaces, which depend on the highly flexible Complementarity-Determining Regions of antibodies[42,43]. MetaESI avoids this issue by not relying on interface training data.

Ablation studies identified key contributors to interface accuracy (Supplementary Fig. 6). GARD was the most critical factor for E3-interface prediction, likely by enforcing lock-and-key complementarity to identify structured binding sites. In contrast, substrate-interface accuracy was primarily driven by sequence context, as substrate degrons often form short linear motifs[44] whose recognition depends on the relative positioning of residues. Beyond model architecture, the strategy for constructing biologically meaningful negative datasets is crucial for accurate interface prediction. To address this, we adopted

https://doi.org/10.1038/s41467-026-73143-8

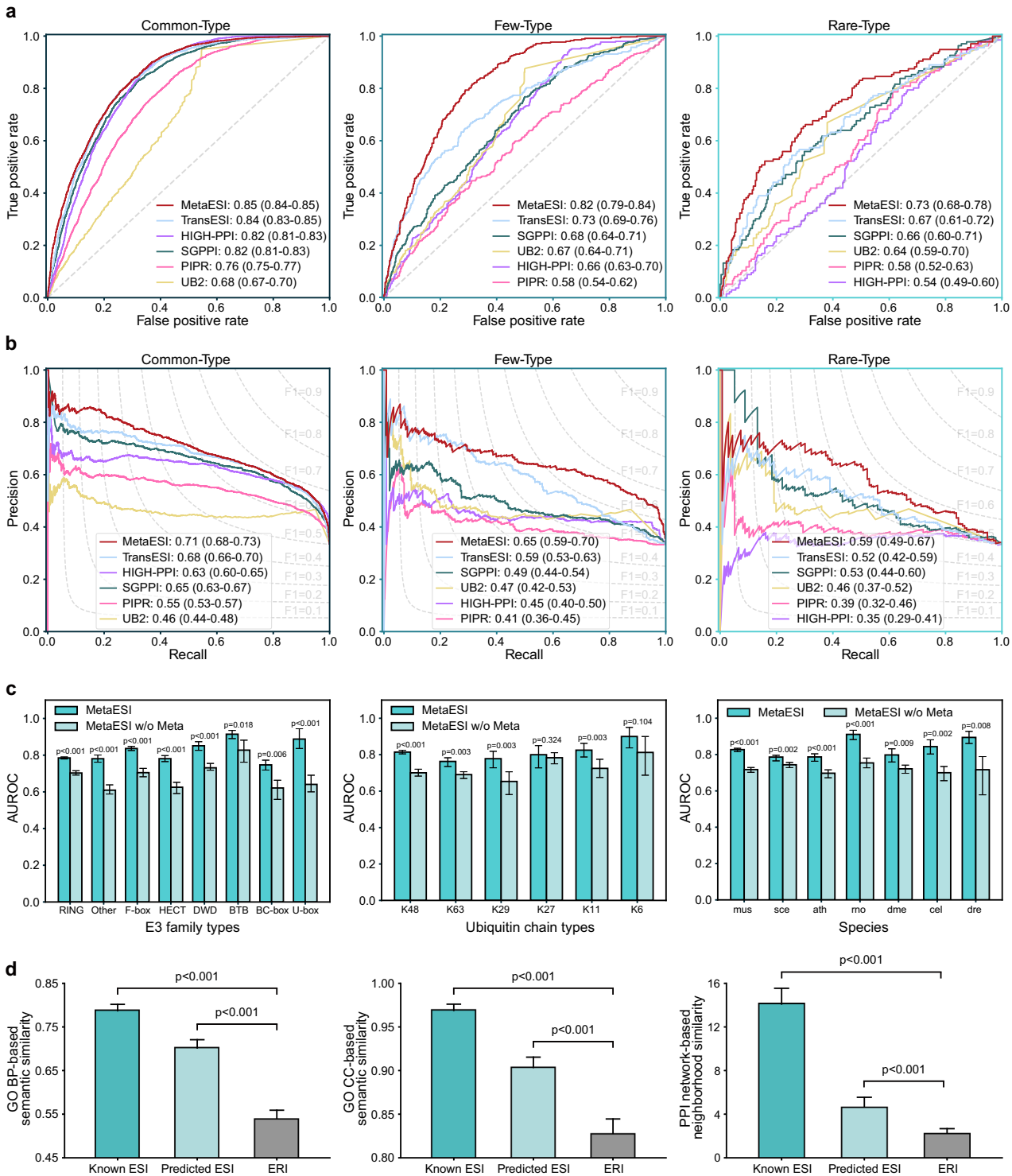

an E3-centric and substrate-centric balanced sampling strategy (Supplementary Fig. 7 and "Methods"). This approach ensured that the Gold Standard Negative (GSN) datasets matched the GSP datasets in connectivity, meaning that each E3 or substrate had a similar number of interactors. For example, SPOP interacts with 41 known substrates. If negative examples are undersampled, MetaESI may spuriously associate SPOP's presence with binding. Imbalanced sampling induced clear interpretability artifacts. Substrate-centric imbalance skewed attention to substrate features (vertical interface map stripes; Supplementary Fig. 8a), while E3-centric imbalance overemphasized E3 features (horizontal stripes; Supplementary Fig. 8b). Only balanced GSN data yielded biologically meaningful interaction patterns (Supplementary Fig. 8c).

Leveraging MetaESI's high-accuracy interface predictions, we augmented the MetaESI-Atlas with residue-level interfaces. This enhanced version now annotates binding interfaces for all 68,056 E3–substrate pairs (Supplementary Data 1).

MetaESI decodes oncogenic substrate-interface mutations disrupting proteostasis in cancer

Oncogenic substrate-interface mutations drive tumorigenesis by impairing ubiquitin-mediated proteostasis, resulting in pathological

Fig. 2 | Performance evaluation of MetaESI. a, **b** Performance evaluation of various models in predicting ESIs across Common-Type (left), Few-Type (middle), and Rare-Type E3s (right). The ROC curves illustrate model performance with TPR (true positive rate) versus FPR (false positive rate) (**a**) and the PR curves display precision versus recall (**b**). The 95% confidence intervals were calculated using bias-corrected and accelerated (BCa) bootstrap resampling ($n = 1000$ iterations). The reference line indicates a non-informative prediction with an AUROC of 0.5 (**a**) or a prediction with a constant F1 score across different thresholds (**b**). Axis border colors correspond to E3 types. **c** Performance comparison of MetaESI and its non-meta-learning counterpart (MetaESI w/o Meta) in predicting ESIs across different E3 family types (left), ubiquitin chain types (middle), and species (right). Bar heights represent mean AUROC values calculated from 10 independent experimental repeats, with error bars indicating 95% confidence intervals calculated through BCa bootstrap resampling ($n = 1000$ iterations). Statistical significance was assessed by one-tailed paired *t*-tests comparing MetaESI with MetaESI w/o Meta for each category. Species abbreviations: mus (*M. musculus*), sce (*S. cerevisiae*), ath (*A. thaliana*), rno (*R. norvegicus*), dme (*D. melanogaster*), cel (*C. elegans*), dre (*D. rerio*). **d** Comparison of functional association features among known ESIs ($n = 1000$), predicted ESIs ($n = 1000$), and random E3-non-substrate interactions (ERIs, $n = 1000$). Three key metrics are shown: GO BP-based semantic similarity (left), GO CC-based semantic similarity (middle), and PPI network-based neighborhood similarity (right). Colored bars represent mean similarity scores, with error bars denoting 95% confidence intervals (calculated as mean ± 1.96 × SEM). One-tailed Mann–Whitney *U* tests assess differences between ERIs and both known and predicted ESIs. ERIs were randomly sampled from non-ESI PPIs to serve as negative controls. Source data are provided as a Source Data file.

stabilization of oncoproteins[3]. To systematically identify substrate-interface mutations that disrupt proteostasis, we developed a three-step framework. First, MetaESI predicts upstream E3s and residue-level binding interfaces for any protein, allowing classification of mutations as interface or non-interface (Fig. 4a). Second, we quantify mutation-induced stabilization by training regression models on tumor samples to predict expected protein abundance from mRNA levels (Fig. 4b and Supplementary Data 5). The deviation between predicted and observed abundance provides a measure of stability change[45]. Third, we prioritize potential driver mutations[46] by requiring both tumor-specific protein accumulation and functional dependency, as assessed by DepMap[47] CRISPR screens (see "Methods").

Applying this framework to 46,062 somatic mutations across 14,617 proteins from 1064 CPTAC tumor samples[48,49] identified 162 mutations with significant stabilization effects (Supplementary Data 6), among which 28 also showed oncogenic accumulation and dependency (Fig. 4c and Supplementary Fig. 9). Among these, the JunB Q244E variant in head and neck squamous cell carcinoma (HNSCC) showed the most pronounced stabilization effect (Supplementary Data 7).

JunB, a transcription factor regulating proliferation and apoptosis[50], displayed significant accumulation in HNSCC tumors relative to normal tissues and conferred strong growth dependency in corresponding cell lines (Fig. 4c). The Q244E mutation significantly enhanced JunB accumulation in mutant versus wild-type HNSCC tumors (Fig. 4d). MetaESI mapped this mutation to the COP1-binding interface (241-EEPQTVP-247; Fig. 4e), indicating that Q244E disrupts COP1-mediated ubiquitination. This mechanism likely drives JunB accumulation, promoting oncogenic progression in HNSCC.

To validate the MetaESI-predicted interaction and ubiquitin ligase activity between COP1 and JunB, we performed co-immunoprecipitation (Co-IP) and in vivo ubiquitination assays. The former confirmed their physical interaction, and the latter demonstrated that COP1 mediates the ubiquitination of JunB (Fig. 4f). Furthermore, the predicted COP1-binding region in JunB was found to be vital for this interaction, as deletion of the motif (241-EEPQTVP-247) abolished COP1-binding and reduced JunB ubiquitination (Fig. 4g). Critically, the JunB Q244E mutation identified in HNSCC patients disrupted the interaction with COP1 and significantly diminished COP1-mediated ubiquitination (Fig. 4h). To assess the functional consequence of disrupted ubiquitination, we generated stable HN30 cell lines overexpressing wild-type JunB or the Q244E mutant. Both cell lines exhibited significantly increased migratory capacity compared to controls. Notably, the Q244E mutant induced a stronger pro-migratory effect than wild-type JunB (Fig. 4i, j and Supplementary Fig. 10). Conversely, overexpression of COP1 increased JunB ubiquitination, reduced JunB protein abundance, and thereby suppressed cell migration, whereas JunB Q244E expression was resistant to COP1-mediated degradation and sustained high migratory capacity (Fig. 4i, j and Supplementary Fig. 10). Structural modeling revealed that wild-type residue Q244 inserts deeply into the central cavity of the COP1 WD40 domain (Supplementary Fig. 11). The Q244E substitution is interpreted to sterically hinder this deep insertion, explaining the disruption of COP1–JunB binding observed experimentally.

Beyond JunB, further analysis of the 162 proteostasis-disrupting substrate-interface mutations revealed that Cyclin D1 (CCND1) mutations in uterine corpus endometrial carcinoma (UCEC) showed the most pronounced effects (Supplementary Fig. 12a). CCND1, a key regulator of G1/S transition, transcription, and DNA repair[51], demonstrated significantly elevated protein stability in five mutant tumors compared to 24 wild-type samples within the CPTAC UCEC cohort (Supplementary Fig. 12b). Crucially, all five mutations clustered within the MetaESI-predicted FBXO31-binding interface, a computational prediction independently validated by an existing crystal structure (PDB: 5VZU[52]; Supplementary Fig. 12c). This suggests that CCND1 interface mutations impair FBXO31 recognition, disrupting ubiquitination and thereby stabilizing CCND1.

These findings demonstrate that MetaESI, combined with multi-omics analysis, provides a systematic approach to uncover substrate-interface mutations that impair proteostasis and drive tumorigenesis.

MetaESI decodes oncogenic E3-interface mutations rewiring ESI networks in cancer

We next extended our framework to mutations in E3 ligases themselves, which can rewire entire substrate networks by dysregulating all proteins that interact through the affected interface[53]. We define such cases as oncogenic E3s (OncoE3s). To detect OncoE3s, we applied three criteria: (1) annotation of E3 mutations as interface or non-interface using MetaESI predictions (Fig. 5a), (2) assessment of cancer-type-specific positive selection[54,55] by testing for enrichment of interface mutations[56,57] compared to germline variants (Fig. 5b, c), and (3) quantification of oncogenic impact using established driver significance metrics[55] (see "Methods").

Across 35,055 somatic missense mutations in 371 E3s from TCGA[58], this analysis identified 1279 mutations within predicted E3 interfaces (Supplementary Data 8). Prioritization based on positive selection and oncogenic impact highlighted SPOP in prostate adenocarcinoma (PRAD) and FBXW7 in UCEC as top OncoE3s (Fig. 5d and Supplementary Data 9).

In PRAD, recurrent SPOP mutations (Y87, F102, W131, F133) clustered within MetaESI-predicted binding interfaces for multiple predicted substrates, including EGR1 (Fig. 5e). Structural modeling of the SPOP–EGR1 complex confirmed Y87, F102, W131, and F133 form the physical binding interface with EGR1 475–481 (Fig. 5f), suggesting that mutations at these sites may impair substrate recognition. We propose these mutations rewire ESI networks by disrupting degradation of multiple oncogenic substrates like EGR1, a prioritized candidate due to its established role in prostate cancer growth[59].

To validate the MetaESI predictions, we performed Co-IP and ubiquitination assays, which confirmed that SPOP interacts with and

https://doi.org/10.1038/s41467-026-73143-8

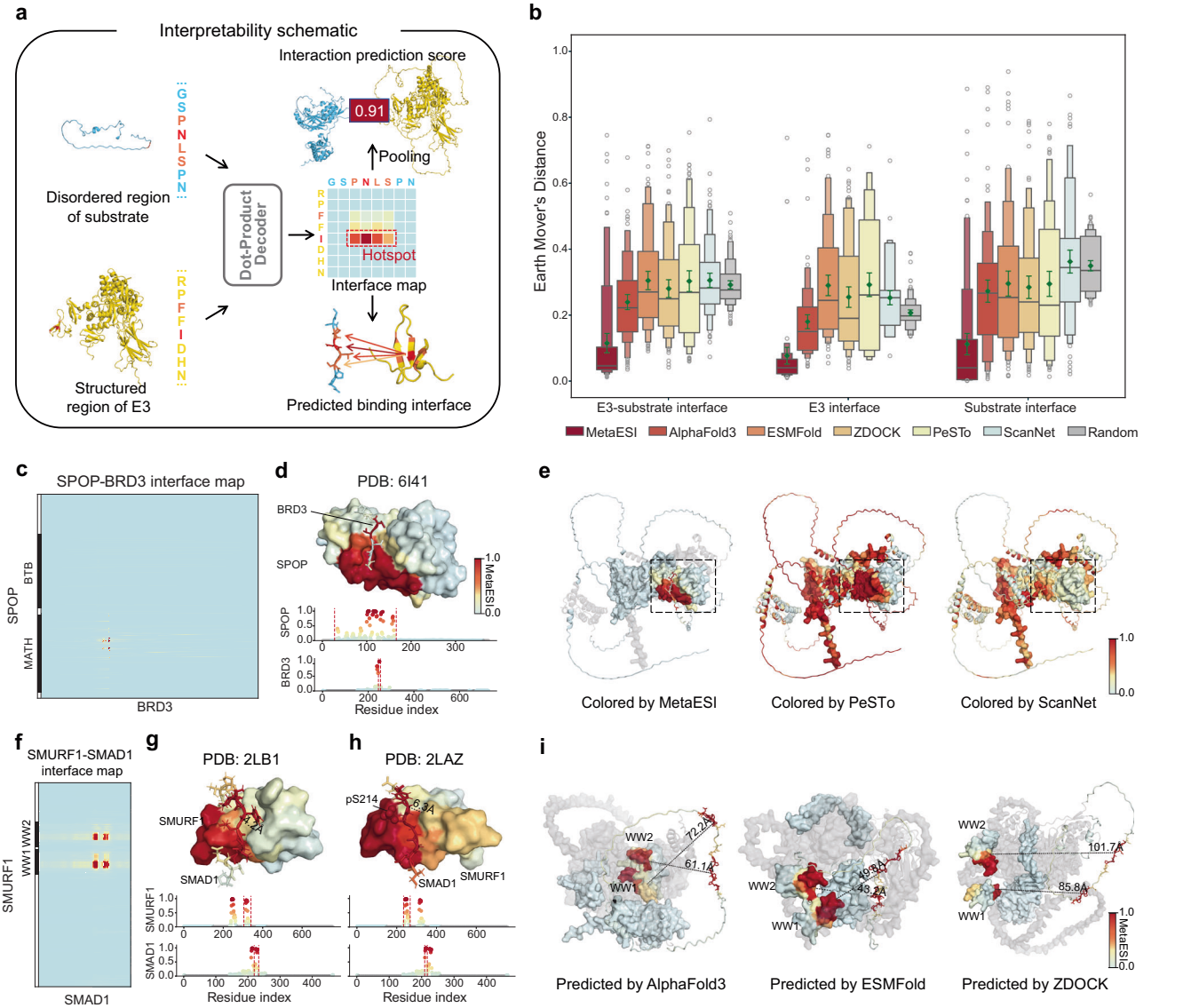

Fig. 3 | MetaESI interpretability and performance. a Schematic of MetaESI's interpretability framework. E3–substrate pairs are processed to generate a pairwise residue interaction probability matrix (interface map), with E3 residues as rows and substrate residues as columns. High-probability hotspots are aggregated via max-pooling to obtain MetaESI Scores (e.g., 0.91), reflecting ESI probabilities. These hotspots also highlight putative binding interface residues. Residue-level MetaESI Scores are derived by projecting maximum interface probabilities onto individual E3 or substrate residues. **b** Letter-value plots comparing EMD distributions between predicted and ground truth interfaces across three levels ($n = 791$ each): full interface (2D), E3 (1D projection), and substrate (1D projection). Plots show median, interquartile range, and progressively extreme percentiles; whiskers extend toward distribution tails. Means (green diamonds) and 95% confidence intervals are indicated. **c** Interface map for SPOP–BRD3, with residues of BRD3 (*x*-axis) and SPOP (*y*-axis) and annotated SPOP domains. **d** Top: SPOP–BRD3 structure (PDB: 6I41; SPOP surface, BRD3 sticks) colored by residue-level scores. Bottom: corresponding score profiles. Red dashed lines indicate experimentally determined regions. **e** AlphaFold3-predicted full-length SPOP–BRD3 structure colored by MetaESI (left), PeSTo (middle), and ScanNet (right). Black dashed boxes denote experimentally resolved regions (PDB: 6I41). **f** Interface map for SMURF1–SMAD1 with annotated SMURF1 domains. **g** Top: SMURF1–SMAD1 complex (PDB: 2LB1) colored by MetaESI. Bottom: score profiles with experimentally defined interfaces (red dashed lines). **h** Alternate SMURF1–SMAD1 structure (PDB: 2LAZ) highlighting phosphorylated S214 (sphere) and corresponding score profiles. **i** Predicted SMURF1–SMAD1 complexes from AlphaFold3, ESMFold, and ZDOCK, colored by MetaESI scores. Black dashed lines connect closest interface residue pairs from (**g** and **h**) to visualize the spatial distances between the experimentally validated interface residues within the predicted models. In (**e** and **i**), gray shading indicates regions excluded by the GARD metric as non-interfacial, corresponding to IDRs on the E3 and structured regions of the substrate.

ubiquitinates EGR1 (Fig. 5g). The PRAD-recurrent SPOP F102C mutation significantly impaired both SPOP–EGR1 binding and EGR1 ubiquitination (Fig. 5g). Consistently, deletion of the predicted SPOP-binding motif (residues 475–481) in EGR1 abolished SPOP binding and reduced EGR1 ubiquitination (Fig. 5h). These results closely matched with the MetaESI predictions. Functionally, while EGR1 overexpression enhanced the migration of DU145 cells, co-expression of wild-type SPOP suppressed migration by promoting EGR1 ubiquitination and degradation (Fig. 5i–k). In contrast, SPOP F102C failed to rescue this phenotype, sustaining migratory capacity.

Similarly, recurrent FBXW7 interface mutations (G423, R465, R479, R505) in UCEC impaired recognition of oncogenic substrates, including CCNE1, validated through MetaESI-predicted and crystallographic interfaces (PDB: 2OVQ[60]; Supplementary Fig. 13).

These results illustrate how MetaESI-guided analysis of E3-interface mutations can reveal oncogenic network rewiring

https://doi.org/10.1038/s41467-026-73143-8

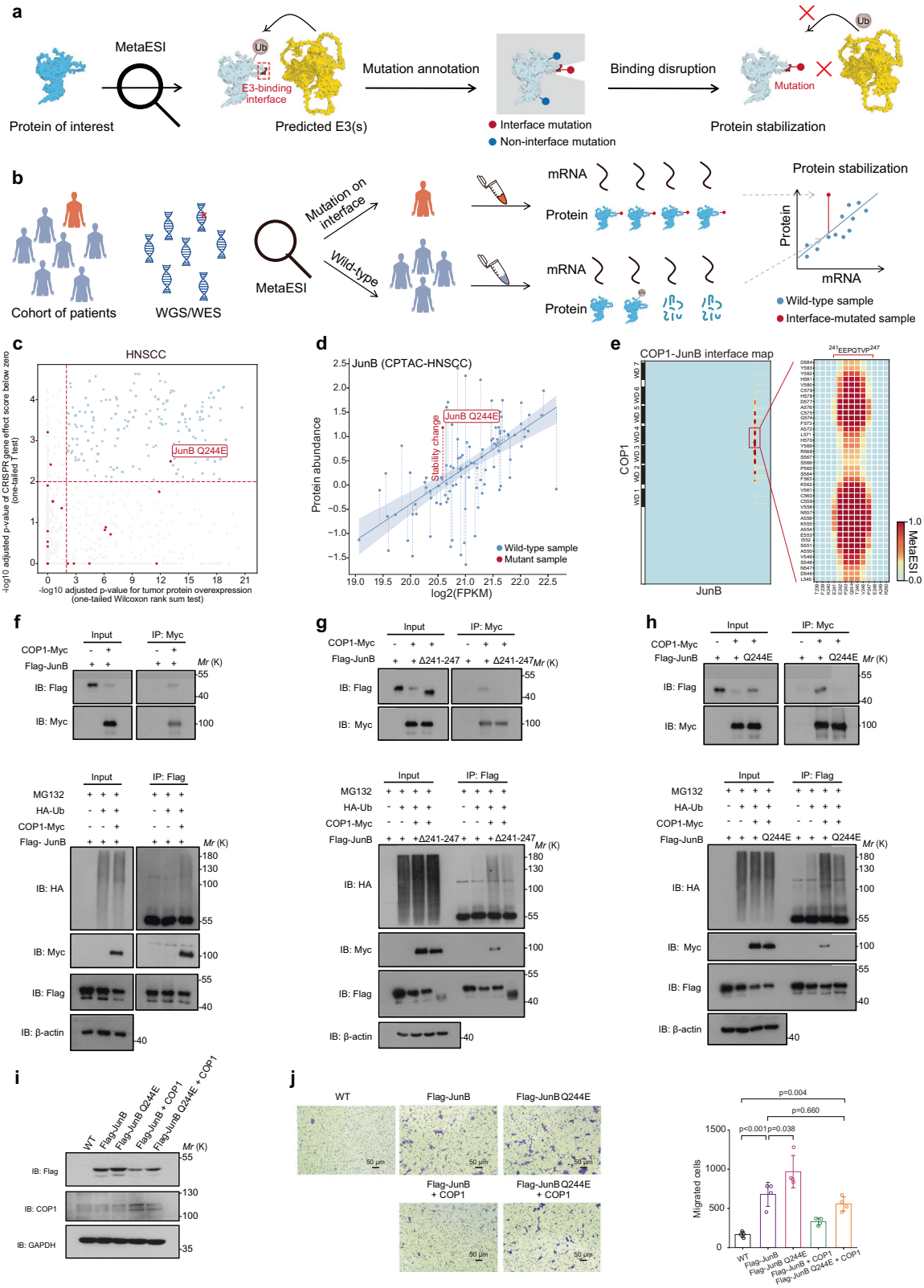

mechanisms, offering a systematic route to identify E3s whose dysregulated interfaces represent potential therapeutic vulnerabilities.

Discussion

Deep learning has shown remarkable potential for deciphering biomolecular interactions, yet most models remain black boxes that provide little mechanistic insight. To overcome this limitation, we designed MetaESI as an intrinsically interpretable framework that embeds biological principles directly into its architecture. This design not only achieves high predictive accuracy but also enables de novo inference of binding interfaces, thereby moving beyond association toward mechanistic understanding.

MetaESI's design philosophy represents a fundamental methodological advance. Early studies (e.g., UbiBrowser) relied on manually

Fig. 4 | MetaESI-guided identification and experimental validation of oncogenic substrate-interface mutations. a Workflow for mutation annotation. MetaESI predicts E3(s) and the E3-binding interfaces for a protein of interest (POI), classifying mutations as interface or non-interface. Interface mutations are expected to disrupt E3 binding and ubiquitination, resulting in protein stabilization. **b** Quantification of mutation-induced protein stabilization. Whole-genome/exome sequencing (WGS/WES) data are analyzed to stratify samples into wild-type and interface-mutant groups. A regression model relating mRNA expression (*x*-axis) to protein abundance (*y*-axis) is fitted using wild-type samples (blue). Deviation of interface-mutant samples (red) from expected values reflects stabilization. **c** Scatter plot of mutation oncogenic potential in HNSCC. Each point represents a mutation, positioned by proteomic significance (*x*-axis) and CRISPR knockout dependency (*y*-axis). MetaESI-predicted substrate-interface mutations are highlighted (red). Mutations exceeding both thresholds ($P < 0.01$; dashed lines) are annotated. **d** mRNA–protein relationship for JunB in HNSCC. Wild-type samples (blue; $n = 105$) define the regression model; the interface-mutant sample (red; $n = 1$) shows elevated protein abundance relative to expectation. Shaded band indicates the 95% confidence interval of the fitted model. **e** MetaESI interface map for COP1–JunB, with COP1 (*y*-axis) and JunB (*x*-axis) residues. The boxed region (COP1 L545–D584; JunB T238–R250) highlights the predicted binding interface. **f**–**h** Co-immunoprecipitation and ubiquitination assays in HEK293T cells expressing COP1 and wild-type or mutant JunB (Δ241–247 or Q244E) assess protein interaction and ubiquitination. **i** Immunoblot analysis in HN30 cells with lentiviral overexpression of COP1 and either JunB or JunB Q244E examines protein abundance. Each experiment was independently repeated three times with similar results. **j** Transwell assays in the same cells evaluate migration capacity. Scale bar, 50 μm. Data are shown as mean ± 1.96 × SEM ($n = 4$). Statistical significance was determined by one-way ANOVA with Tukey's HSD test. Source data are provided as a Source Data file.

defined statistical features (e.g., enriched domain pairs and motifs), whose interpretability was constrained by predefined assumptions and data distributions, limiting their capacity to reveal universal biological mechanisms. Subsequent deep learning models (e.g., TransDSI/TransESI) relied on conjoint triad encodings and *post hoc* explanation, restricting interpretability to isolated residues. In contrast, MetaESI integrates biological constraints into its architecture, providing intrinsic interpretability. Instead of highlighting isolated residues, it infers coordinated residue–residue contacts and structured interface patterns, thereby capturing the mechanistic basis of E3–substrate recognition.

Leveraging MetaESI's predictive and interpretative capabilities, we constructed the MetaESI-Atlas, a comprehensive E3–substrate interactome with residue-level interface annotations for humans and seven model organisms (Supplementary Data 1). Through integrated multi-omics analysis of this atlas, we identified proteostasis-disrupting substrate-interface mutations (Supplementary Data 6) and ESI-network-rewiring E3-interface mutations (Supplementary Data 8) in cancer. Experimental validation confirmed representative oncogenic mechanisms. The JunB Q244E mutation drives HNSCC by disrupting binding to the E3 COP1, while the SPOP F102C mutation promotes PRAD by impairing binding to its EGR1 substrate. This atlas bridges cancer genomics and precision oncology by systematically linking mutation hotspots, substrate dysregulation, and oncogenic phenotypes.

Beyond ubiquitination biology, MetaESI offers a generalizable framework for interpretable bioinformatics. Its architecture is readily adaptable to other pairwise prediction problems (e.g., antigen–antibody or protein–peptide binding) by incorporating domain-specific knowledge. Furthermore, its two-stage learning strategy offers a viable solution for data-scarce biological tasks by transferring knowledge from large-scale, biologically relevant prediction tasks. Looking ahead, MetaESI's meta-learning architecture could also be extended to predict functional attributes of interactions, such as the ubiquitin chain types assembled during substrate ubiquitination, once sufficient high-quality annotations become available. Moreover, MetaESI's precise interface definitions significantly improved AlphaFold's modeling of specific E3–substrate complexes (e.g., SPOP–EGR1; Fig. 5f), in stark contrast to failures observed when using full-length sequences as input (Supplementary Fig. 14).

As high-throughput sequencing advances and large-scale genomic/exome projects expand across diseases, we believe MetaESI-Atlas will be a powerful resource for discovering diverse disease-relevant interface mutations. We have made the MetaESI-Atlas and full model code publicly available (https://github.com/LiDlab/MetaESI). This open resource aims to: (1) facilitate the identification of candidate E3s and substrates for ubiquitination studies, (2) advance understanding of ubiquitin-mediated proteostasis and its dysregulation in disease through interface characterization, and (3) catalyze the translation of fundamental insights into clinical applications.

Methods

Gold standard positive dataset construction

The gold standard positive dataset of ESIs was curated from our UbiBrowser 2.0[16] database. Each interaction pair was manually verified and supported by well-documented literature evidence. First, we collected all the literature published from 1982 to 2021 that may involve E3 and substrate interactions from PubMed containing the following keyword combinations: ("ubiquitin ligase" OR "ubiquitin ligases" OR "E3 ligase" OR "E3 ligases") AND ("substrate" OR "substrates"). Next, three experienced researchers independently screened all candidate abstracts to extract known ESIs through manual curation. Potential ESIs were manually filtered and verified based on the following textual patterns: "E ubiquitylates S…", "E mediates the ubiquitination of S…", "E targets S for ubiquitination…", "E promotes the proteasome degradation of S…", "E plays a crucial role in the ubiquitination of S…", "S is the substrate of E…", "S is ubiquitinated and degraded by E…", or "S is resistant to degradation mediated by E…", where E is an E3 and S is a substrate. The final GSP dataset comprises 3534 manually curated ESIs spanning eight species, of which 2640 are human. Each ESI is annotated with supporting evidence for the ubiquitination relationship between E3 and substrate (Supplementary Data 2).

Gold standard negative dataset construction

We constructed the GSN dataset using a two-stage, topology-preserving sampling strategy to address key limitations in previous negative sampling methods[61–63]. High-confidence PPIs, with a confidence score > 300, were first extracted from STRING[64] v11.5 to establish a candidate pool. To ensure systematic coverage of both E3 and substrate specificities, we implemented the following critical strategies (Supplementary Fig. 7): (1) E3-centric sampling: For each E3, we randomly selected non-substrate interactors from the PPI network, while maintaining the E3's degree (i.e., matching the number of its known substrates in GSP dataset). (2) Substrate-centric sampling: For each substrate, we similarly sampled non-regulator E3s while preserving its interaction degree. The GSN dataset was compiled by combining these two subsets, ensuring no overlap with known ESIs or between sampling stages, and was further curated to maintain a 1:2 ratio (GSP:GSN) for each species in the GSP dataset (Supplementary Data 2). We utilized a group-stratified splitting approach, ensuring that matched GSP–GSN pairs were consistently assigned to the same data partition. This mitigated potential data imbalance in the training and evaluation stages.

Protein feature extraction

To characterize protein features, predicted structures of reference proteomes from multiple species and their corresponding PAE files

https://doi.org/10.1038/s41467-026-73143-8

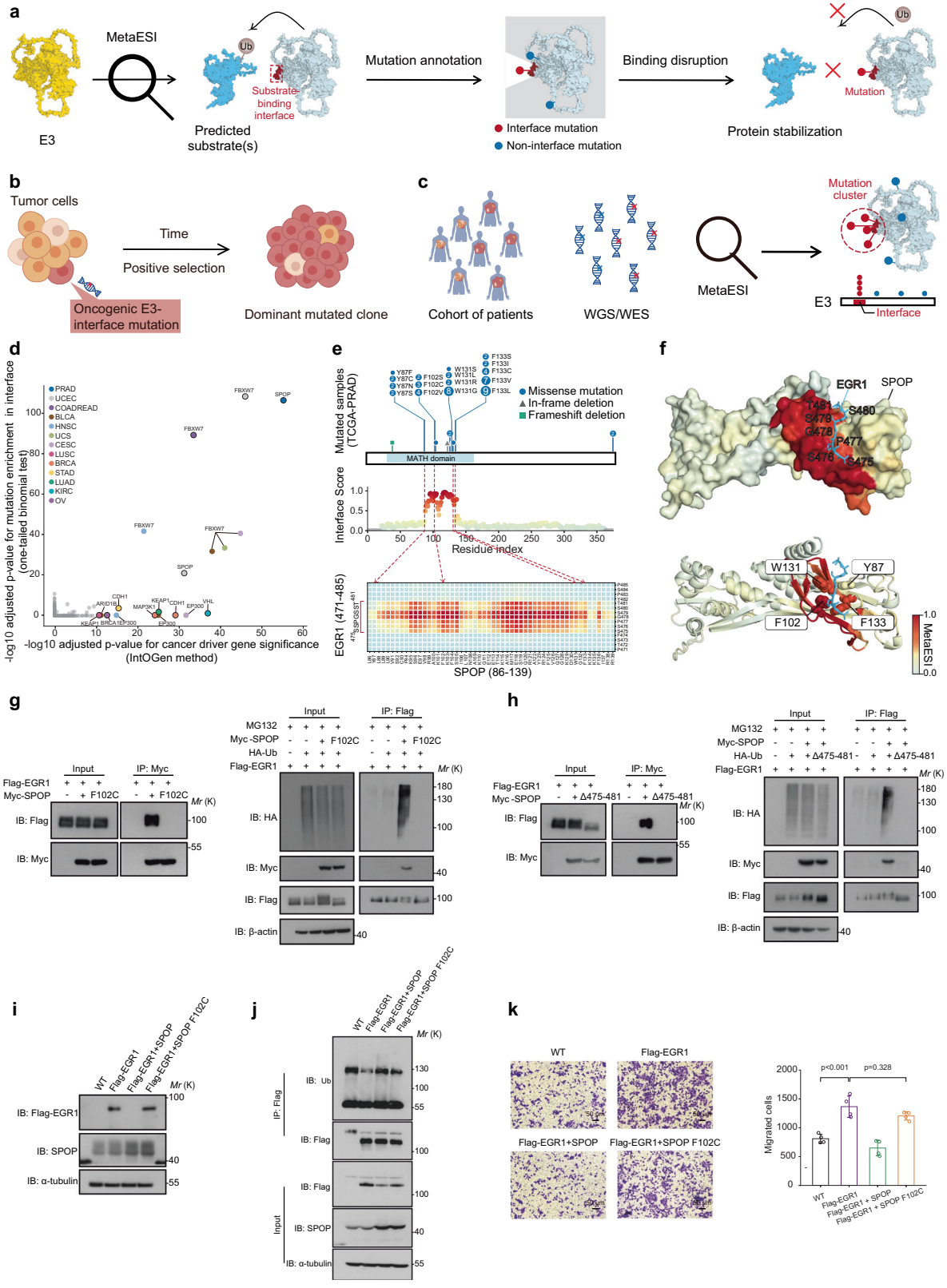

in JSON format were obtained from the AlphaFold Database. Protein sequences were extracted from the structures using Biopython and subsequently encoded by the ESM2 model to generate residue-level representations from its 33rd layer as sequence features. Disordered properties were calculated using the GARD metric based on the AlphaFold2-predicted structures and PAE data (see Supplementary Methods). We systematically identified conformationally stable regions (GARD > 1.5) in E3s and dynamic disordered segments (GARD ≤ 1.5) in substrates. For E3s, residues within stable regions (GARD > 1.5) were selected, and residue contact maps were constructed using a Cα–Cα distance threshold of 9 Å. For substrates, dynamic disordered fragments (GARD ≤ 1.5) were filtered, retaining only residue features located within these fragments.

Fig. 5 | MetaESI-guided identification and experimental validation of oncogenic E3-interface mutations. a Workflow for mutation annotation. MetaESI predicts substrate(s) and substrate-binding interfaces for an E3, classifying mutations as interface or non-interface. Interface mutations are expected to disrupt substrate binding and ubiquitination, resulting in protein stabilization. **b** Model of clonal expansion driven by oncogenic E3-interface mutations. A tumor cell harboring an interface mutation (red) undergoes positive selection, leading to dominance of the mutated clone. **c** Cohort-level enrichment of E3-interface mutations. Tumors are stratified by mutation status, with interface mutations (red) enriched at predicted binding interfaces, whereas other mutations are broadly distributed. **d** Enrichment of somatic interface mutations (*y*-axis) versus cancer driver effects (*x*-axis) across 6359 cancer type–E3 pairs. Gray points indicate low driver significance ($x < 10$); colored points indicate high driver significance ($x \geq 10$). Black borders denote Cancer Gene Census-annotated driver E3s. **e** Mutational landscape of SPOP in prostate adenocarcinoma (TCGA-PRAD; $n = 62$). Top: Lollipop plot of SPOP somatic mutations (symbols denote mutation types; numbers indicate sample counts). Middle: MetaESI interface scores along SPOP residues (dashed red line: hotspot mutation positions). Bottom: Predicted interface map between SPOP (86–139) and EGR1 (471–485). **f** Predicted SPOP–EGR1 structure (EGR1 residues 475–481). Top: SPOP surface with EGR1 (sticks). Bottom: SPOP cartoon highlighting hotspot mutations (spheres: Y87, F102, W131, F133). **g**, **h** Co-immunoprecipitation and ubiquitination assays in HEK293T cells expressing wild-type or mutant SPOP (F102C) and EGR1 (wild-type or Δ471–485) assess protein interaction and ubiquitination. **i** Immunoblot analysis in DU145 cells with lentiviral overexpression of EGR1 and either wild-type or mutant SPOP examines protein abundance. **j** Ubiquitination assays in the same cells following MG132 treatment assess EGR1 ubiquitination. Each experiment was independently repeated three times with similar results. **k** Transwell assays in the same cells evaluate migration capacity. Scale bar, 50 μm. Data are shown as mean ± 1.96 × SEM ($n = 4$). Statistical significance was determined by one-way ANOVA with Tukey's HSD test. Source data are provided as a Source Data file.

MetaESI architecture

The MetaESI framework integrates a truncated Transformer[25] with a GAT[26] to model ESIs. The GAT processes structured regions on the E3 (represented as a graph), while the Transformer handles disordered regions of the substrate. Below, we formalize the key components.

Graph attention network for E3 processing. The E3 is represented as a graph $G = (V, E)$, where nodes V correspond to residues with features $\mathbf{h}_i \in \mathbb{R}^{1280}$. A three-layer multi-head GAT hierarchically aggregates structural information from neighboring residues:

$$\mathbf{h}_i^{(l)} = \Big\|_{k=1}^{K_l} \mathrm{LeakyReLU}\left(\sum_{j \in N(i)} \alpha_{ij}^{k,l} \mathbf{W}^{k,l} \mathbf{h}_j^{(l-1)}\right) \tag{1}$$

with attention coefficients $\alpha_{ij}^{k,l}$ computed as:

$$\alpha_{ij}^{k,l} = \mathrm{softmax}_j\left(\mathrm{LeakyReLU}\left(\mathbf{a}^{l^T}\left[\mathbf{W}^{k,l}\mathbf{h}_i^{(l-1)} \| \mathbf{W}^{k,l}\mathbf{h}_j^{(l-1)}\right]\right)\right) \tag{2}$$

where $N(i)$ denotes neighbors of residue i, $\|$ indicates concatenation, and K_l is the number of attention heads in layer l. The first layer uses 4 heads (32 features per head, total 128), while subsequent layers use 2 heads (32 features per head, total 64). The final E3 representation $\mathbf{E3} \in \mathbb{R}^{n \times 256}$ is obtained by concatenating outputs of all three layers (128 + 64 + 64), capturing both local and global structural features.

Truncated transformer for substrate processing. The substrate disordered region $\mathbf{S} = \{\mathbf{s}_1, \ldots, \mathbf{s}_m\}$, with residue features $\mathbf{s}_i \in \mathbb{R}^{1280}$, is processed via a multi-head truncated Transformer designed to capture local motifs. For each head k, residue features are linearly projected into query ($\mathbf{Q}$), key ($\mathbf{K}$), and value ($\mathbf{V}$) matrices:

$$\mathrm{head}_k = \mathrm{Attention}\left(\mathbf{SW}_k^Q, \mathbf{SW}_k^K, \mathbf{SW}_k^V\right),\ \mathbf{W}_k^Q, \mathbf{W}_k^K, \mathbf{W}_k^V \in \mathbb{R}^{1280 \times 32} \tag{3}$$

The attention mechanism is constrained by a local window attention mask $\mathbf{M} \in \mathbb{R}^{m \times m}$, which restrict interactions to a sliding window of $w = 7$ residues:

$$\mathbf{M}_{ij} = \begin{cases} 0 & \text{if} |i-j| \leq \lfloor w/2 \rfloor \\ -\infty & \text{otherwise} \end{cases} \tag{4}$$

This local attention enables the model to focus on short-range dependencies critical for motif detection. The attention function is computed as:

$$\mathrm{Attention}(\mathbf{Q}, \mathbf{K}, \mathbf{V}) = \mathrm{softmax}\left(\mathbf{QK}^T/\sqrt{\mathrm{d}_k} + \mathbf{M}\right)\mathbf{V},\ \mathrm{d}_k = 32. \tag{5}$$

Outputs from $h = 8$ parallel heads are concatenated and transformed:

$$\mathbf{x} = \mathrm{LayerNorm}\left(\mathrm{Concat}(\mathrm{head}_1, \ldots, \mathrm{head}_h)\mathbf{W}^O\right),\ \mathbf{W}^O \in \mathbb{R}^{256 \times 256}. \tag{6}$$

A residual feed-forward network further refines $\mathbf{x}$ to produce the final substrate representation $\mathbf{SUB} \in \mathbb{R}^{m \times 256}$:

$$\mathbf{SUB} = \mathrm{LayerNorm}(\mathbf{x} + \mathrm{ReLU}(\mathbf{xW}_1)\mathbf{W}_2) \tag{7}$$

where $\mathbf{W}_1 \in \mathbb{R}^{256 \times 512}$ and $\mathbf{W}_2 \in \mathbb{R}^{512 \times 256}$.

Interface map decoder and ESI score prediction. The interface map $\mathbf{I}_{\mathrm{map}} \in \mathbb{R}^{n \times m}$ is computed via a dot-product decoder:

$$\mathbf{I}_{\mathrm{map}} = \mathrm{Sigmoid}\left(\mathbf{E3} \cdot \mathbf{SUB}^T\right) \tag{8}$$

Here, $\mathbf{I}_{\mathrm{map}}$ represents residue-level interaction probabilities between n E3 residues and m substrate residues. The raw ESI probability is derived by applying global max-pooling to $\mathbf{I}_{\mathrm{map}}$:

$$p = \max_{x,y}\left(\mathbf{I}_{\mathrm{map}}^{xy}\right) \tag{9}$$

To calibrate p into the final *MetaESI score*, we apply a unified transformation:

$$\mathit{MetaESI\ score} = \frac{1}{1 + \sqrt{(1-p)/p}} \tag{10}$$

This transformation involves converting the raw probability p into log-odds, followed by non-linear scaling using a sigmoid-like function to map the result into the interval [0, 1]. This ensures the *MetaESI score* reflects a calibrated probability of interaction while maintaining interpretability.

MetaESI learning setting

The MetaESI learning framework comprises two sequential stages: a meta-learning stage and an E3-specific transfer learning stage.

Meta-learning stage. In this stage, the MetaESI model is defined as a function f_θ with parameters θ. The objective of this stage is to train a meta-learner with parameters θ, enabling it to rapidly adapt to new E3-specific ESI prediction tasks by fine-tuning with limited samples. Specifically, the meta-learning process consists of an inner loop and an outer loop. The inner loop focuses on learning individual tasks and optimizing task-specific parameters θ_i. The outer loop focuses on learning across tasks and optimizing the meta-learner's parameters θ

through cross-task gradient aggregation. Assuming the gold standard dataset represents the distribution of E3-specific tasks $P(T)$, the update process for θ is as follows:

First, a batch of training tasks $T_i \sim P(T)$ is randomly sampled to form a training unit called an episode. Each task T_i consists of a support set S_i and a query set Q_i. Within the inner loop, for a specific task T_i, the meta-learner's parameters θ are copied to obtain the initial parameters θ' for the task-specific learner $f_{\theta'}$. The loss $L_{S_i}(f_{\theta'})$ of $f_{\theta'}$ on the support set S_i is calculated, and task-specific parameters θ_i are updated via gradient descent:

$$\theta_i = \theta' - \alpha \cdot \nabla'_{\theta} L_{S_i}(f_{\theta'}) \tag{11}$$

where α is the inner loop learning rate, and $\nabla_{\theta'} L_{S_i}(f_{\theta'})$ denotes the gradient of the training loss for task T_i. For multiple tasks within an episode, the inner loop generates multiple θ_i.

Within the outer loop, the meta-parameters θ are updated by aggregating losses of all task-specific learners f_{θ_i} on their respective query sets Q_i:

$$\theta \leftarrow \theta - \beta \cdot \nabla_{\theta} \sum_{T_i \sim P(T)} L_{Q_i}\left(f_{\theta_i}\right) \tag{12}$$

where $\sum_{T_i \sim P(T)} L_{Q_i}\left(f_{\theta_i}\right)$ represents the total loss across all tasks in the episode, and β is the outer loop learning rate. Through alternating updates of the inner and outer loops, the final parameters θ are optimized to achieve cross-task generalization.

In the meta-learning stage, MetaESI is trained for 10,000 episodes. Each episode samples 10 distinct E3-specific tasks. Both the support set S_i and query set Q_i for each task comprise 6 samples (2 positive and 4 negative) to ensure a consistent number of samples across tasks. The inner loop learning rate α is set to 0.05, and the outer loop learning rate β is set to 1e-4. The inner learning rate is set higher to allow rapid task-specific adaptation within each task, while the lower outer learning rate ensures stable meta-updates that preserve transferable knowledge shared across tasks. The binary cross-entropy loss is employed as the loss function L, and the Adam optimizer is used for training.

E3-specific transfer learning stage. The objective of this stage is to fine-tune the meta-learner by using tailored learning strategies to obtain E3-specific learners with reliable performance for individual E3s. This fine-tuning process closely mirrors the inner loop procedure of the meta-learning stage. Specifically, E3s are categorized into distinct types according to the number of available substrate samples, and differentiated transfer learning strategies are applied to each type.

For common-type E3s (with abundant substrates), we employ many-shot learning: the meta-learner is retrained 100 times using their substrate data. For few-type E3s (limited substrates), the meta-learner is fine-tuned 10 times with their substrate data to derive E3-specific learners, termed few-shot learning. For rare-type E3s (defined as those with only a single known substrate in the dataset), we simulate a challenging orphan E3 scenario: their sole known substrate is withheld for evaluation, and no direct training data from the target E3 is used. Instead, we leverage a similarity-based sampling strategy by computing cosine similarity between rare-type and other E3s using TransDSI embeddings. TransDSI, a framework developed by our team for DSI prediction, integrates sequence features and protein similarity networks to generate embeddings. These embeddings more effectively capture protein family relationships among E3s compared to ESM2 and CT[65] encodings (Supplementary Fig. 15). For each orphan E3, the 8 most similar E3s are identified, and 6 samples (2 positive and 4 negative) per E3 are used to fine-tune the meta-learner 10 times. We term this strategy similarity-based few-shot adaptation, as it adapts the meta-learner to rare-type E3s by leveraging similarity-based sampling from related E3s, despite the absence of direct training data for the target orphan E3s. In all three learning strategies, the learning rate is set to 1e-4 to preserve transferable knowledge from the meta-learner. Optimization employed mini-batch gradient descent (batch size = 4) for many-shot learning and stochastic gradient descent for few-shot and similarity-based adaptation.

Evaluation of ESI prediction performance

To systematically evaluate the predictive capability of MetaESI across three distinct scenarios, we stratified the gold-standard dataset into three subsets based on E3 type: Common, Few, and Rare categories. A group-stratified splitting strategy was implemented to ensure that matched GSP–GSN pairs were consistently assigned to the same data partition throughout the evaluation process. For the Common type dataset, model performance was assessed using fivefold cross-validation, while leave-one-out cross-validation was employed for both Few and Rare type datasets due to their limited sample sizes.

In the fivefold cross-validation procedure, the Common type dataset was randomly divided into five approximately equal subsets. The model underwent five independent training-testing cycles, with each fold sequentially serving as the test set while the remaining four folds constituted the training set. To obtain comprehensive performance metrics, prediction results from all five test folds were aggregated. The area under the receiver operating characteristic curve (AUROC) and area under the precision-recall curve (AUPRC) were subsequently calculated through a unified evaluation process that consolidated all test predictions, thereby providing robust performance estimates across the complete dataset.

Comparative analysis was performed between MetaESI and existing state-of-the-art approaches, including two specialized ESI prediction tools developed by our team (UbiBrowser2.0 and TransESI), as well as general PPI prediction methods (HIGH-PPI, SGPPI, and PIPR). Specifically, HIGH-PPI is a hierarchical graph framework designed to predict types of PPIs by integrating protein structural features and PPI networks. To adapt HIGH-PPI for ESI prediction, we reframed its task as a binary classification problem designed to distinguish specialized ESIs from generic PPIs. SGPPI, our previously developed structure-aware prediction framework, employs multiple sequence features coupled with structural information for PPI inference. For fair comparison with MetaESI, we enhanced SGPPI by replacing conventional sequence features with more expressive embeddings from the ESM2 protein language model.

To investigate the performance drivers of MetaESI, we constructed four ablation variants: (1) MetaESI w/o Seq: A version excluding sequence context, implemented by permuting residue features across the sequence; (2) MetaESI w/o 3D: A structure-agnostic variant where the original residue contact map was replaced with a banded matrix encoding only sequential adjacency (i.e., $i \pm 1$ connectivity), thereby restricting GAT aggregation to sequential neighbors; (3) MetaESI w/o GARD: A version omitting the GARD metric, thus bypassing the exclusion of disordered regions on E3s and structured regions on substrates; (4) MetaESI w/o Meta: A variant trained without the meta-learning stage.

Evaluation of E3–substrate interface prediction performance

To systematically evaluate the performance of E3–substrate interface prediction, we constructed a comprehensive E3–substrate binding interface dataset encompassing both degrons on substrates and substrate-binding regions on E3s (Supplementary Data 4). Degron data were primarily curated from the "DEG"-annotated short linear motifs in the ELM[17] database (Eukaryotic Linear Motif resource), supplemented with manually extracted literature-derived instances. Substrate-binding interfaces on E3s were exclusively compiled through literature mining. This dataset enables comprehensive evaluation of

prediction accuracy at the E3–substrate interface level, as well as independent assessments for E3 or substrate components.

Prediction accuracy was quantified using EMD[36], which assesses spatial discrepancies between predicted and ground truth binding regions. For interface-level evaluation, the MetaESI-predicted interface map $\mathbf{I}_{\text{map}} \in \mathbb{R}^{n\times m}$, representing residue-level interaction probabilities between n E3 residues (rows) and m substrate residues (columns), was converted into an EMD signature:

$$\sigma\left(\mathbf{I}_{\text{map}}\right) = \left\{ \left(\mathbf{I}_{\text{map}}^{xy}, x, y\right) \mid \mathbf{I}_{\text{map}}^{xy} \neq 0 \right\} \tag{13}$$

Here, x and y represent the residue positions on the E3 and substrate, respectively. The 2D EMD between the predicted map $\mathbf{I}_{\text{map}}$ and ground truth $\mathbf{I}_{\text{gt}}$ was computed as:

$$\text{EMD}_{\text{2D}} = \frac{\min_{flow} \sum_{i\in\sigma(\mathbf{I}_{\text{map}}), j\in\sigma(\mathbf{I}_{\text{gt}})} flow[i,j] \cdot \sqrt{\left(x_i - x_j\right)^2 + \left(y_i - y_j\right)^2}}{\sqrt{(n-1)^2 + (m-1)^2}} \tag{14}$$

where $flow[i,j]$ represents the optimal transport flow from position i in $\mathbf{I}_{\text{map}}$ to position j in $\mathbf{I}_{\text{gt}}$, and the denominator provides normalization by the maximum theoretical 2D spatial distance.

In addition to the interface-level evaluation using 2D EMD, we also employed 1D EMD for component-specific assessments. For component-specific evaluation (e.g., E3-level), a 1D EMD was calculated by projecting the interface maps onto the E3 axis. The row-wise maximum projection $P_{E3}(\mathbf{I})$ for a map $\mathbf{I}$ is defined as:

$$P_{E3}(\mathbf{I}) = \left[\max_{y} \mathbf{I}[x, y]\right]_{x=1}^{n} \tag{15}$$

The 1D EMD between projected predictions $P_{E3}\left(\mathbf{I}_{\text{map}}\right)$ and ground truth $P_{E3}\left(\mathbf{I}_{\text{gt}}\right)$ is:

$$\text{EMD}_{\text{E3}} = \frac{\min\limits_{flow} \sum_{i\in 1P_{E3}(\mathbf{I}_{\text{map}}), j\in P_{E3}(\mathbf{I}_{\text{gt}})} flow[i,j] \cdot |i-j|}{n-1} \tag{16}$$

where $flow[i,j]$ represents the optimal transport flow from position i in $P_{E3}\left(\mathbf{I}_{\text{map}}\right)$ to position j in $P_{E3}\left(\mathbf{I}_{\text{gt}}\right)$. $|i-j|$ is the 1D distance between positions i and j, and the denominator provides normalization by the maximum possible distance along the E3 axis.

We benchmarked MetaESI against state-of-the-art methods, including two protein complex structure prediction tools (AlphaFold3[23] and ESMFold[24]), a structure-based protein docking method (ZDOCK[34]), and two structure-based binding site prediction methods (PeSTo[37] and ScanNet[38]). For AlphaFold3, ESMFold, and ZDOCK, we generated interface maps by calculating all pairwise Euclidean distances between Cα atoms of residues in chain A (E3) and chain B (substrate) from predicted protein complex structures. A binary matrix $\mathbf{I}_{\text{map}}$ was constructed, where elements were assigned 1 if the inter-residue distance was <6 Å (indicating potential interactions) and 0 otherwise. For PeSTo and ScanNet, which predict binding sites from monomeric structures, we generated interface maps by selecting the top 10 ranked residues on both E3 and substrate based on their predicted binding scores. Smaller 2D EMD or 1D EMD values indicate closer alignment between predicted and ground truth binding regions, reflecting higher predictive accuracy.

E3–substrate interaction and binding interface prediction

To support direct application in research, we constructed the MetaESI-Atlas through MetaESI-driven proteome-wide screening. We focused on E3s with experimentally supported ubiquitin ligase activity (curated from UbiBrowser and literature for each species) to ensure the functional relevance and reliability of predicted interactions. The selection of the MetaESI score threshold for defining high-confidence ESIs was determined through fivefold cross-validation. Specifically, we identified the minimal threshold (0.749) that achieved a precision exceeding 0.72, thereby prioritizing reliable predictions while retaining balanced sensitivity.

To annotate binding interface residue information for each predicted ESI in MetaESI-Atlas, we developed a residue screening pipeline leveraging the inherently interpretable interface map ($\mathbf{I}_{\text{map}} \in \mathbb{R}^{n\times m}$) generated by the MetaESI framework. This matrix represents residue-level interaction probabilities between n residues of the E3 and m residues of the substrate. To pinpoint critical interface residues, we first identify all hotspot residue pairs (x,y) using a hotspot-defining threshold:

$$H = \left\{ (x, y) \mid \mathbf{I}_{\text{map}}^{xy} > p - \tau \right\} \tag{17}$$

where $\tau = 0.1$, and p is the raw ESI probability calculated from global max-pooling (Eq. (14)). Based on H, residues are ranked descendingly by their $\mathbf{I}_{\text{map}}$ values, and we select the top 20 unique E3 residues and top 10 unique substrate residues with the highest contributions to the interaction. For the E3, the interface residues are defined as:

$$\text{R}_{\text{E3}}^{\text{interface}} = \left\{ x_1, \ \ldots, x_{20} \mid (x_k, y_k) \in H, \mathbf{I}_{\text{map}}^{x_k y_k} \text{sorted descending} \right\} \tag{18}$$

Similarly, for the substrate, the interface residues are defined as:

$$\text{R}_{\text{Sub}}^{\text{interface}} = \left\{ y_1, \ \ldots, y_{10} \mid (x_k, y_k) \in H, \mathbf{I}_{\text{map}}^{x_k y_k} \text{sorted descending} \right\} \tag{19}$$

For structural visualization (e.g., Supplementary Fig. 11), continuous per-residue interaction scores are mapped onto the protein surface, whereas the definitively predicted interface residues are strictly the top-scoring subset defined in Eqs. (18 and 19).

To investigate the biological properties of MetaESI-Atlas, we performed functional association analysis between E3s and their substrates based on GO semantic similarity. Semantic similarity scores for GO terms of paired proteins were computed with the R package GOSemSim[66]. Furthermore, a PPI network was constructed based on interactions derived from STRING v11.5. Neighborhood similarity within the PPI network was quantified by calculating the statistical significance of shared interaction partners between protein pairs using Fisher's exact test. The resulting P-values were transformed into a similarity metric, which is defined as the PPI network-based neighborhood similarity.

Identifying oncogenic substrate-interface mutations

We obtained and processed multi-omics data from the Clinical Proteomic Tumor Analysis Consortium (CPTAC[48]) Pan-Cancer Dataset, including proteomic profiles, RNA-seq, somatic mutation data, and copy number alterations (CNA) across 1064 tumor samples spanning 10 cancer types. Molecular identifiers were standardized to RefSeq IDs using BioMart mapping files, yielding 9,278,112 protein-sample pairs covering 14,617 unique proteins.

For each protein-cancer type pair, the relationship between protein abundance (quantified by mass spectrometry, MS) and mRNA expression (log2-transformed FPKM values) was assessed via iteratively reweighted least squares regression. Samples harboring somatic mutations, high-level amplifications (CNA ≥ 2), or alterations in upstream E3s were excluded from regression analysis. Associations were retained only if the filtered sample size exceeded 10, resulting in 104,846 RNA-protein correlations (Supplementary Data 5). High-confidence associations were defined as those with a weighted correlation coefficient > 0.3 for downstream stability change calculations.

Protein stability changes were quantified using regression residuals. Raw residuals (vertical distance between observed protein abundance and predicted values from mRNA levels) were normalized by the ratio of mRNA expression standard deviation (σ_{mRNA}) to protein

abundance standard deviation (σ_{MS}):

$$\text{Stability change} = \frac{\text{Raw residual} \times \sigma_{mRNA}}{\sigma_{MS}} \quad (20)$$

To evaluate the impact of missense mutations on protein stability, stability changes in mutated samples were compared to the mean stability change in wild-type samples. Significance was assessed via two-sided one-sample Student's *t*-tests, with *P*-values adjusted using the Benjamini–Hochberg (BH) method. This analysis identified 46,062 mutations altering protein stability (Supplementary Data 6).

Substrate-interface mutations were annotated using the MetaESI-Atlas and GSP datasets to map upstream E3s and their binding interfaces. Among 431 interface mutations, 162 significantly increased protein stability (BH-adjusted $P < 0.01$) and were defined as proteostasis-disrupting substrate-interface mutations, while 163 decreased stability (BH-adjusted $P < 0.01$).

To characterize the oncogenic potential of substrate-interface mutations, we implemented a two-step analytical framework. First, proteomic data from the CPTAC database were analyzed to identify tumor-specific protein overexpression using a one-tailed Wilcoxon rank-sum test (tumor > normal), followed by BH adjustment (BH-adjusted $P < 0.01$). Second, CRISPR-Cas9 dependency scores from the Cancer Dependency Map (DepMap[47]) were employed to prioritize proteins critical for cancer cell survival and proliferation, applying a one-tailed Student's *t*-tests (dependency score <0) with BH correction (BH-adjusted $P < 0.01$). Proteins that showed both significant tumor overexpression and functional essentiality were classified as high-confidence oncoproteins. Mutations located within substrate interfaces of these proteins were defined as oncogenic substrate-interface mutations (Supplementary Data 7).

Identifying oncogenic E3-interface mutations

We obtained somatic mutations from the cBioPortal[67] database, encompassing 32 cancer types in the TCGA Pan-Cancer Atlas cohort (COAD and READ combined). After filtering, 35,055 somatic missense mutations across 371 E3s were retained. Germline missense mutations for these E3s were sourced from the gnomAD[68] database as a population background ($n = 121{,}782{,}867$). E3-interface mutations were annotated using the MetaESI-Atlas and GSP datasets to map downstream substrates and their binding interfaces (Supplementary Data 8).

For each cancer type-E3 pair ($n = 6359$), we quantified somatic interface and non-interface mutations by grouping TCGA data by cancer type and E3. Germline interface and non-interface allele counts were aggregated by E3 from gnomAD. To assess enrichment of somatic interface mutations, a one-sided binomial test was performed comparing the somatic interface mutation proportion against the germline background proportion, with germline interface mutation frequency as the expected probability. Resulting *P*-values underwent BH false discovery rate correction. We then integrated TCGA driver gene annotations from IntOGen and cancer driver genes from the Cancer Gene Census to identify E3s whose interface mutations confer cancer-driving effects (termed OncoE3; Supplementary Data 9).

Plasmids and cell culture

Full-length cDNAs encoding COP1, SPOP, and SPOP F102C were cloned into the pCMV-Myc vector. And full-length cDNAs encoding JunB, JunB Q244E, and EGR1 were cloned into the pFlag-CMV-2 vector.

HEK293T (ATCC, CRL-3216), DU145(ATCC, HTB-81), and HN30 (Pricella, CL-0799) cells were maintained in DMEM (YEASEN, 41401ES7) supplemented with 10% fetal bovine serum (FBS; Vazyme, F101-02) and 1% penicillin/streptomycin (Cell world, C0160-611). All cell lines were cultured at 37 °C in containing 5% CO_2.

Cell transfections, lentivirus packaging, and infection

HEK293T cells were transfected with the indicated plasmids using Lipofectamine 2000 (Invitrogen, 11668019) according to the manufacturer's protocol. Full-length cDNAs encoding COP1, SPOP, or SPOP F102C were cloned into the pCDH-puro lentiviral vector, while full-length cDNAs encoding JunB, JunB Q244E, or EGR1 were cloned into the pLV3-CMV-MCS-GFP-EF1a-Puro lentiviral vector. Subsequently, the respective transfer plasmid was co-transfected with the packaging plasmid pSPAX.2 and the envelope plasmid pMD.2 G into HEK293T cells at a ratio of 4:3:1. Viral supernatant was collected at 36, 48, and 60 h post-transfection and filtered through a 0.22-μm filter. The filtered viral supernatant was then mixed 1:1 with DMEM medium and used to infect HN30 or DU145 cells.

Co-immunoprecipitation and immunoblotting

HEK293T cells were co-transfected with the indicated plasmids for 48 h. Subsequently, cells were lysed in HEPES lysis buffer (20 mM HEPES, pH 7.2, 50 mM NaCl, 0.5% Triton ×-100, 1 mM NaF) supplemented with a protease inhibitor cocktail (MCE, HYK0010) and a phosphatase inhibitor (Solarbio, P1260). Cell lysates were incubated with anti-Flag (1:300; MBL, M185-3L) or anti-Myc (1:500; MBL, M192-3) antibodies for 8 h at 4 °C, followed by incubation with 50 μL of Protein A/G agarose beads (Santa Cruz, sc-2003) for an additional 8 h. The beads were then washed three times with HEPES lysis buffer. Finally, the immunocomplexes bound to the beads were resuspended in 2× loading buffer (100 mM Tris, 200 mM dithiothreitol, 10% SDS, 0.2% bromophenol blue, and 20% glycerol, pH 6.8) and boiled for 15 min. Both whole-cell lysates and immunoprecipitated complexes were analyzed by immunoblotting.

Protein samples were separated by SDS-PAGE and electrophoretically transferred onto nitrocellulose (NC) membranes (Merck Millipore, Germany). Then, the membranes were blocked with 5% skim milk in Tris-buffered saline containing 0.1% Tween-20 (TBST) for 1 h at room temperature. Subsequently, the membranes were incubated overnight at 4 °C with the indicated primary antibodies, the antibodies were purchased from the following sources and used at the indicated dilutions: Flag (1:4000; MBL, M185-3L), Myc (1:4000; MBL, M192-3), Flag-HRP (1:1500; MCE, F1105), α-tubulin (1:10,000; Proteintech, 66031-1-Ig), GAPDH (1:10,000; Abclonal; A19056), β-actin (1:20,000; Abclonal; AC028), Ubiquitin (1:1000; MBL; D058-3), COP1 (1:1000; ABclonal, A22106) and SPOP (1:500; Proteintech; 16750-1-AP). After primary antibody incubation, the membranes were washed three times (10 min per wash) with TBST. Next, the membranes were incubated with appropriate horseradish peroxidase (HRP)-conjugated secondary antibodies diluted in blocking buffer for 1 h at room temperature and washed three times (10 min per wash) with TBST. Finally, immunoreactive bands were visualized using Western Bright ECL chemiluminescent detection reagent (Thermo Fisher Scientific).

In vivo ubiquitination assay

HEK293T cells were co-transfected with HA-ubiquitin and the indicated plasmids using Lipofectamine 2000. Forty hours post-transfection, cells were treated with 20 μM MG132 (HY-13259, MCE) diluted in DMEM medium for 8 h. Cells were then lysed in RIPA lysis (50 mM Tris-HCl, pH 7.4, 150 mM NaCl, 5 mM EDTA, 1% NP-40) buffer supplemented with a protease inhibitor cocktail (MCE, HYK0010) and a phosphatase inhibitor (Solarbio, P1260). For immunoprecipitation, cell lysates were incubated with the appropriate primary antibody for 8 h at 4 °C, followed by incubation with Protein A/G agarose beads (Santa Cruz, sc-2003) for an additional 8 h at 4 °C. The beads were subsequently washed three times with RIPA lysis buffer. Immunoprecipitated proteins were analyzed by immunoblotting.

Cell migration assay

For cell migration assays, the indicated cells (2×10^5 cells/chamber) were plated in the upper chamber of a 24-well transwell insert with an

8-µm pore polyethylene terephthalate membrane (Corning, 3422). The upper chambers were filled with 150 µL serum-free DMEM, while the lower chambers contained 600 µL DMEM supplemented with 10% FBS. After incubation at 37 °C with 5% CO_2 for 12 or 36 h, non-migrated cells on the upper membrane surface were removed by gentle scraping with a cotton swab. The migrated cells on the lower surface were then fixed with 4% formaldehyde for 15 min at room temperature, washed with PBS, and stained with 0.1% crystal violet for 20 min. Following another PBS wash and air-drying, the membranes were imaged under a bright-field microscope. Quantification of the migrated cells number was performed using ImageJ. Results are represented as the mean ± s.e.m. of three technical repeats.

Reporting summary

Further information on research design is available in the Nature Portfolio Reporting Summary linked to this article.

Data availability

The datasets supporting this study were sourced from publicly available repositories: protein–protein interactions from STRING; E3–substrate interactions from UbiBrowser 2.0 (http://ubibrowser.bio-it.cn/ubibrowser_v3/); protein sequences and domain annotations from UniProt (https://www.uniprot.org/); predicted protein structures and corresponding PAE data from the AlphaFold Protein Structure Database (https://alphafold.ebi.ac.uk/); experimentally determined protein structures (PDB: 6I41, 2LB1, 2LAZ, 5VZU, 2OVQ); intrinsically disordered region data from DisProt (https://disprot.org/); degron motif instances from the ELM; multi-omics data from the CPTAC Pan-Cancer Dataset (https://pdc.cancer.gov/pdc/cptac-pancancer); gene knockout phenotype data from DepMap (https://depmap.org/); somatic mutation data (32 cancer types, TCGA Pan-Cancer Atlas; COAD/READ combined) accessed via cBioPortal (https://www.cbioportal.org/); human population germline variation data from gnomAD (https://gnomad.broadinstitute.org/); and cancer driver gene annotations from IntOGen (https://www.intogen.org/). The data generated in this study is provided in the Supplementary Data files. Source data are provided with this paper.

Code availability

The source code of MetaESI is packaged as π-MetaESI and available at GitHub https://github.com/LiDlab/MetaESI and Zenodo https://zenodo.org/records/16730897[69].

References

1. Hipp, M. S., Kasturi, P. & Hartl, F. U. The proteostasis network and its decline in ageing. *Nat. Rev. Mol. Cell Biol.* **20**, 421–435 (2019).
2. Buetow, L. & Huang, D. T. Structural insights into the catalysis and regulation of E3 ubiquitin ligases. *Nat. Rev. Mol. Cell Biol.* **17**, 626–642 (2016).
3. Mészáros, B., Kumar, M., Gibson, T. J., Uyar, B. & Dosztányi, Z. Degrons in cancer. *Sci. Signal.* **10**, eaak9982 (2017).
4. Zhang, Z., Mena, E. L., Timms, R. T., Koren, I. & Elledge, S. J. Degrons: defining the rules of protein degradation. *Nat. Rev. Mol. Cell Biol.* **26**, 868–883 (2025).
5. Senft, D., Qi, J. & Ronai, Z. A. Ubiquitin ligases in oncogenic transformation and cancer therapy. *Nat. Rev. Cancer* **18**, 69–88 (2018).
6. Eifert, C. & Powers, R. S. From cancer genomes to oncogenic drivers, tumour dependencies and therapeutic targets. *Nat. Rev. Cancer* **12**, 572–578 (2012).
7. Rodriguez, H., Zenklusen, J. C., Staudt, L. M., Doroshow, J. H. & Lowy, D. R. The next horizon in precision oncology: proteogenomics to inform cancer diagnosis and treatment. *Cell* **184**, 1661–1670 (2021).
8. Carr, T. H. et al. Defining actionable mutations for oncology therapeutic development. *Nat. Rev. Cancer* **16**, 319–329 (2016).
9. Nero, T. L., Morton, C. J., Holien, J. K., Wielens, J. & Parker, M. W. Oncogenic protein interfaces: small molecules, big challenges. *Nat. Rev. Cancer* **14**, 248–262 (2014).
10. Tang, C. et al. Hypomorph mutation-directed small-molecule protein-protein interaction inducers to restore mutant SMAD4-suppressed TGF-β signaling. *Cell Chem. Biol.* **28**, 636–647.e5 (2021).
11. Tsai, J. M., Nowak, R. P., Ebert, B. L. & Fischer, E. S. Targeted protein degradation: from mechanisms to clinic. *Nat. Rev. Mol. Cell Biol.* **25**, 740–757 (2024).
12. Aloy, P. & Russell, R. B. Structural systems biology: modelling protein interactions. *Nat. Rev. Mol. Cell Biol.* **7**, 188–197 (2006).
13. Moreira, I. S., Fernandes, P. A. & Ramos, M. J. Hot spots—A review of the protein–protein interface determinant amino-acid residues. *Proteins Struct. Funct. Bioinforma.* **68**, 803–812 (2007).
14. Li, Y. et al. An integrated bioinformatics platform for investigating the human E3 ubiquitin ligase-substrate interaction network. *Nat. Commun.* **8**, 347 (2017).
15. Liu, Y. et al. A protein sequence-based deep transfer learning framework for identifying human proteome-wide deubiquitinase-substrate interactions. *Nat. Commun.* **15**, 4519 (2024).
16. Wang, X. et al. UbiBrowser 2.0: a comprehensive resource for proteome-wide known and predicted ubiquitin ligase/deubiquitinase-substrate interactions in eukaryotic species. *Nucleic Acids Res.* **50**, D719–D728 (2022).
17. Kumar, M. et al. ELM-the eukaryotic linear motif resource-2024 update. *Nucleic Acids Res.* **52**, D442–D455 (2024).
18. Elmarakeby, H. A. et al. Biologically informed deep neural network for prostate cancer discovery. *Nature* **598**, 348–352 (2021).
19. Novakovsky, G., Dexter, N., Libbrecht, M. W., Wasserman, W. W. & Mostafavi, S. Obtaining genetics insights from deep learning via explainable artificial intelligence. *Nat. Rev. Genet.* **24**, 125–137 (2023).
20. Klauschen, F. et al. Toward explainable artificial intelligence for precision pathology. *Annu. Rev. Pathol. Mech. Dis.* **19**, 541–570 (2024).
21. Chen, V. et al. Applying interpretable machine learning in computational biology—pitfalls, recommendations and opportunities for new developments. *Nat. Methods* **21**, 1454–1461 (2024).
22. He, F. et al. π-HuB: the proteomic navigator of the human body. *Nature* **636**, 322–331 (2024).
23. Abramson, J. et al. Accurate structure prediction of biomolecular interactions with AlphaFold 3. *Nature* **630**, 493–500 (2024).
24. Lin, Z. et al. Evolutionary-scale prediction of atomic-level protein structure with a language model. *Science* **379**, 1123–1130 (2023).
25. Yeh, C.-F. et al. Transformer-transducer: end-to-end speech recognition with self-attention. Preprint at https://doi.org/10.48550/arXiv.1910.12977 (2019).
26. Veličković, P. et al. Graph attention networks. Preprint at https://doi.org/10.48550/arXiv.1710.10903 (2018).
27. Vendruscolo, M., Kussell, E. & Domany, E. Recovery of protein structure from contact maps. *Fold. Des.* **2**, 295–306 (1997).
28. Ma, J. et al. Few-shot learning creates predictive models of drug response that translate from high-throughput screens to individual patients. *Nat. Cancer* **2**, 233–244 (2021).
29. Gao, Y. et al. Pan-peptide meta learning for T-cell receptor–antigen binding recognition. *Nat. Mach. Intell.* **5**, 236–249 (2023).
30. Finn, C., Abbeel, P. & Levine, S. Model-agnostic meta-learning for fast adaptation of deep networks. In *Proceedings of the 34th International Conference on Machine Learning* (ed. Precup, D. & Teh, Y. W.) 1126–1135 (PMLR, 2017).
31. Gao, Z. et al. Hierarchical graph learning for protein–protein interaction. *Nat. Commun.* **14**, 1093 (2023).
32. Huang, Y., Wuchty, S., Zhou, Y. & Zhang, Z. SGPPI: structure-aware prediction of protein-protein interactions in rigorous conditions with graph convolutional network. *Brief. Bioinform.* **24**, bbad020 (2023).

33. Chen, M. et al. Multifaceted protein-protein interaction prediction based on Siamese residual RCNN. *Bioinformatics* **35**, i305–i314 (2019).
34. Pierce, B. G. et al. ZDOCK server: interactive docking prediction of protein-protein complexes and symmetric multimers. *Bioinformatics* **30**, 1771–1773 (2014).
35. Das, R. & Baker, D. Macromolecular modeling with Rosetta. *Annu. Rev. Biochem.* **77**, 363–382 (2008).
36. Rubner, Y., Tomasi, C. & Guibas, L. J. The earth mover's distance as a metric for image retrieval. *Int. J. Comput. Vis.* **40**, 99–121 (2000).
37. Krapp, L. F., Abriata, L. A., Cortés Rodriguez, F. & Dal Peraro, M. PeSTo: parameter-free geometric deep learning for accurate prediction of protein binding interfaces. *Nat. Commun.* **14**, 2175 (2023).
38. Tubiana, J., Schneidman-Duhovny, D. & Wolfson, H. J. ScanNet: an interpretable geometric deep learning model for structure-based protein binding site prediction. *Nat. Methods* **19**, 730–739 (2022).
39. Ostertag, M. S., Hutwelker, W., Plettenburg, O., Sattler, M. & Popowicz, G. M. Structural insights into BET client recognition of endometrial and prostate cancer-associated SPOP mutants. *J. Mol. Biol.* **431**, 2213–2221 (2019).
40. Zhuang, M. et al. Structures of SPOP-substrate complexes: insights into molecular architectures of BTB-Cul3 ubiquitin ligases. *Mol. Cell* **36**, 39–50 (2009).
41. Aragón, E. et al. A Smad action turnover switch operated by WW domain readers of a phosphoserine code. *Genes Dev.* **25**, 1275–1288 (2011).
42. Yin, R., Feng, B. Y., Varshney, A. & Pierce, B. G. Benchmarking AlphaFold for protein complex modeling reveals accuracy determinants. *Protein Sci.* **31**, e4379 (2022).
43. McCoy, K. M., Ackerman, M. E. & Grigoryan, G. A comparison of antibody–antigen complex sequence-to-structure prediction methods and their systematic biases. *Protein Sci.* **33**, e5127 (2024).
44. Isono, E. et al. Protein degrons and degradation: exploring substrate recognition and pathway selection in plants. *Plant Cell* **36**, 3074–3098 (2024).
45. Martínez-Jiménez, F., Muiños, F., López-Arribillaga, E., Lopez-Bigas, N. & Gonzalez-Perez, A. Systematic analysis of alterations in the ubiquitin proteolysis system reveals its contribution to driver mutations in cancer. *Nat. Cancer* **1**, 122–135 (2020).
46. Savage, S. R. et al. Pan-cancer proteogenomics expands the landscape of therapeutic targets. *Cell* **187**, 4389–4407.e15 (2024).
47. Arafeh, R., Shibue, T., Vazquez, F. & Hahn, W. C. Cancer dependency map: past and present. *Annu. Rev. Cancer Biol.* **9**, 43–57 (2025).
48. Whiteaker, J. R. et al. CPTAC assay portal: a repository of targeted proteomic assays. *Nat. Methods* **11**, 703–704 (2014).
49. Li, Y. et al. Pan-cancer proteogenomics connects oncogenic drivers to functional states. *Cell* **186**, 3921–3944.e25 (2023).
50. Piechaczyk, M. & Farràs, R. Regulation and function of JunB in cell proliferation. *Biochem. Soc. Trans.* **36**, 864–867 (2008).
51. Musgrove, E. A., Caldon, C. E., Barraclough, J., Stone, A. & Sutherland, R. L. Cyclin D as a therapeutic target in cancer. *Nat. Rev. Cancer* **11**, 558–572 (2011).
52. Li, Y. et al. Structural basis of the phosphorylation-independent recognition of cyclin D1 by the SCFFBXO31 ubiquitin ligase. *Proc. Natl. Acad. Sci. USA* **115**, 319–324 (2018).
53. Fu, H., Mo, X. & Ivanov, A. A. Decoding the functional impact of the cancer genome through protein–protein interactions. *Nat. Rev. Cancer* **25**, 189–208 (2025).
54. Zhao, S. et al. Detailed modeling of positive selection improves detection of cancer driver genes. *Nat. Commun.* **10**, 3399 (2019).
55. Martínez-Jiménez, F. et al. A compendium of mutational cancer driver genes. *Nat. Rev. Cancer* **20**, 555–572 (2020).
56. Kamburov, A. et al. Comprehensive assessment of cancer missense mutation clustering in protein structures. *Proc. Natl. Acad. Sci. USA* **112**, E5486–E5495 (2015).
57. Cheng, F. et al. Comprehensive characterization of protein–protein interactions perturbed by disease mutations. *Nat. Genet.* **53**, 342–353 (2021).
58. Cancer Genome Atlas Research Network et al. The Cancer Genome Atlas Pan-Cancer analysis project. *Nat. Genet.* **45**, 1113–1120 (2013).
59. Virolle, T. et al. Egr1 promotes growth and survival of prostate cancer cells. Identification of novel Egr1 target genes. *J. Biol. Chem.* **278**, 11802–11810 (2003).
60. Hao, B., Oehlmann, S., Sowa, M. E., Harper, J. W. & Pavletich, N. P. Structure of a Fbw7-Skp1-cyclin E complex: multisite-phosphorylated substrate recognition by SCF ubiquitin ligases. *Mol. Cell* **26**, 131–143 (2007).
61. Ben-Hur, A. & Noble, W. S. Choosing negative examples for the prediction of protein-protein interactions. *BMC Bioinforma.* **7**, S2 (2006).
62. Park, Y. & Marcotte, E. M. Revisiting the negative example sampling problem for predicting protein–protein interactions. *Bioinformatics* **27**, 3024–3028 (2011).
63. Zahiri, J., Yaghoubi, O., Mohammad-Noori, M., Ebrahimpour, R. & Masoudi-Nejad, A. PPIevo: protein-protein interaction prediction from PSSM based evolutionary information. *Genomics* **102**, 237–242 (2013).
64. Szklarczyk, D. et al. The STRING database in 2021: customizable protein-protein networks, and functional characterization of user-uploaded gene/measurement sets. *Nucleic Acids Res.* **49**, D605–D612 (2021).
65. Shen, J. et al. Predicting protein–protein interactions based only on sequences information. *Proc. Natl. Acad. Sci. USA***104**, 4337–4341 (2007).
66. Yu, G. et al. GOSemSim: an R package for measuring semantic similarity among GO terms and gene products. *Bioinformatics* **26**, 976–978 (2010).
67. Gao, J. et al. Integrative analysis of complex cancer genomics and clinical profiles using the cBioPortal. *Sci. Signal.* **6**, pl1–pl1 (2013).
68. Karczewski, K. J. et al. The mutational constraint spectrum quantified from variation in 141,456 humans. *Nature* **581**, 434–443 (2020).
69. Li, D. MetaESI data. *Zenodo* https://doi.org/10.5281/zenodo.16730897 (2025).

Acknowledgements

We thank Wenyu Shi (China Agricultural University) and Zhongyang Liu (National Center for Protein Sciences, Beijing) for their valuable feedback and insightful discussions.

Author contributions

D.L. (Dianke Li), Y.Z., Y.L., Z.Z. (Ziding Zhang), C.C., and D.L. (Dong Li) conceived and developed the project. D.L. (Dianke Li) and Y.L. developed the models and conducted computational experiments; Y.Z., L.Z., and C.C. designed and conducted biological experiments; D.L. (Dianke Li), Y.Z., Z.Z. (Zihao Zhang), Y.Q., J.L., and L.J. performed the analyses. D.L. (Dianke Li), Y.Z., Z.Z. (Zihao Zhang), Y.Q., J.L., L.J., Y.L., L.D., Z.Z. (Ziding Zhang), C.C., and D.L. (Dong Li) wrote the manuscript. All authors discussed the results and reviewed the manuscript.

Funding

Dong Li discloses support for the research of this work from the National Natural Science Foundation of China (grant number 32271518), the National Key Research and Development Program of China (grant numbers 2024YFA1307703 and 2023YFF1204600), and the National Natural Science Foundation of China (grant number 32088101). Chun-Ping Cui discloses support for the research of this work from the National Key Research and Development Program of China (grant numbers 2022YFC3401500 and 2021YFA1300200). Ziding Zhang discloses support for the research of this work from the National Natural Science Foundation of China (grant number 32270703).

Competing interests
The authors declare no competing interests.

Additional information
Supplementary information The online version contains supplementary material available at https://doi.org/10.1038/s41467-026-73143-8.

Correspondence and requests for materials should be addressed to Ziding Zhang, Lingqiang Zhang, Chun-Ping Cui or Dong Li.

Peer review information *Nature Communications* thanks Wassim Gabriel and the other, anonymous, reviewer(s) for their contribution to the peer review of this work. A peer review file is available.